Astronomy and Computing 55 (2026) 101089

Contents lists available at ScienceDirect

Astronomy and Computing

journal homepage: www.elsevier.com/locate/ascom

Full length paper

Validation of COSMICA code for massive stochastic simulation of cosmic rays propagation in the heliosphere☆

Stefano Della Torre [a,c], Leone Bacciu [b], Matteo Grazioso [b,a], Giovanni Cavallotto [a,c], Massimo Gervasi [a,d], Giuseppe La Vacca [a,d], Sabina Rossi [b], Marco S. Nobile [b,*]

[a] National Institute for Nuclear Physics (INFN), Division of Milano-Bicocca, Piazza della Scienza, 3, Milano (MI), 20126, Italy
[b] Ca' Foscari University of Venice, Department of Environmental Sciences, Informatics and Statistics, Via Torino 155, Venezia Mestre, 30172, Italy
[c] ICSC - Centro Nazionale di Ricerca in HPC, Big Data and Quantum Computing, Via Magnanelli, 2, Casalecchio di Reno, (BO) 40033, Italy
[d] University of Milano-Bicocca, Department of Physics "Giuseppe Occhialini", Piazza della Scienza, 3, Milano, 20126, Italy

ARTICLE INFO

Keywords:
Galactic Cosmic Rays
Heliosphere
SDE
GPU
Parallel computing
Cuda
Solar modulation
Parker Transport Equation
Multi-GPU scalability
CUDA/C++
High-performance computing (HPC)
Space radiation environment

ABSTRACT

The propagation of Galactic Cosmic Rays (GCRs) within the heliosphere is governed by the Parker Transport Equation (PTE), which can be efficiently solved using a Stochastic Differential Equation (SDE)–Monte Carlo formulation. Building upon the first part of this work, where the GPU-based COSMICA code was introduced and optimized for high-performance computing, we here present its validation against a benchmark heliospheric model. COSMICA implements a three-dimensional SDE solver in CUDA/C++ optimized for multi-GPU execution, enabling the simulation of billions of quasi-particle trajectories with unprecedented efficiency. Benchmarking against the closed-source HelMod-4/CUDA model demonstrates that COSMICA achieves runtime reductions exceeding an order of magnitude while maintaining full consistency with reference fluxes. Statistical tests confirm that the distributions of output spectra from COSMICA and HelMod-4/CUDA are indistinguishable within numerical uncertainties. Furthermore, COSMICA enables the analysis of stochastic path properties – such as exit-point distributions, propagation times, and residence times – thereby providing new insights into the modulation process across varying solar activity scenarios. These results establish COSMICA as both computationally superior and scientifically reliable, making it a powerful open-source framework for heliospheric transport studies and a versatile platform for future extensions to more complex physical models.

1. Introduction

From a historical perspective, charged particles coming from outside the Earth (*i.e.*, cosmic rays) represent an invaluable source of discovery and one of the biggest threats in human exploration of space. These particles are mainly composed of protons and helium nuclei, while heavier nuclei contribute only as a minor component. Cosmic rays can be classified by many categories, following energy, composition, and origin, but for the intent of this article, we focus on the Galactic Cosmic Rays (GCR), *i.e.*, those produced outside the Solar System, with supernova remnants regarded as their main sources.

From an applied perspective, GCRs represent a non-negligible radiation hazard for human spaceflight and for spacecraft electronics, making accurate modeling of the space radiation environment essential for planning and risk mitigation (see, *e.g.*, Golge et al., 2015; Samwel et al., 2019; Peter et al., 2022; Rahmanian et al., 2023). From a more fundamental standpoint, precise measurements and theoretical descriptions of GCR spectra are invaluable tools in astroparticle physics: unexpected spectral features may signal the presence of new astrophysical sources (see, *e.g.*, Chang et al., 2008; Abdo et al., 2009; Adriani et al., 2009; Cernuda, 2011; Mertsch and Sarkar, 2011; Della Torre et al., 2015; Rozza et al., 2015; Boschini et al., 2021, 2022b) or reveal physics beyond the standard astrophysical scenario (see, *e.g.*, Bottino et al., 1998; Cirelli and Cline, 2010; Ibarra et al., 2010; Salati, 2011; Weniger, 2011; Alvey et al., 2023).

The solar environment plays a crucial role in GCR propagation from the galaxy toward the Earth: the heliosphere – namely, the vast region shaped by solar activity and enclosing the solar system – acts as a shield that modifies the incoming flux. Once inside this region, GCRs encounter the outward flow of magnetized plasma carried by the solar wind (SW), which results in a time dependent suppression of their intensity compared with the GCR intensity outside the heliosphere (referred in the text as Local Interstellar Spectra – LIS) which is supposed

☆ This article is part of a Special issue entitled: 'HPC in Cosmology and Astrophysics' published in Astronomy and Computing.

* Corresponding author.
E-mail addresses: stefano.dellatorre@mib.infn.it (S. Della Torre), marco.nobile@unive.it (M.S. Nobile).

https://doi.org/10.1016/j.ascom.2026.101089
Received 30 September 2025; Received in revised form 26 December 2025; Accepted 19 February 2026
Available online 25 February 2026

to be isotropic and constant in time. This phenomenon, referred to as *solar modulation*, reflects the variability of solar activity, ranging from short-term fluctuations of days to the quasi-periodic 11-year cycle (22 years when considering the change of Sun magnetic polarity). As a consequence, both the magnitude and the spectral distribution of the cosmic-ray flux observed near Earth are continuously altered by the evolving solar wind and the heliospheric magnetic field (for a review see, *e.g.*, Rankin et al., 2022).

The theoretical framework for describing cosmic-ray propagation inside the heliosphere is provided by the Parker Transport Equation (PTE, Section 2): a Fokker-Plank-like equation that cannot be completely solved without applying numerical methods. Over the last decades, Monte Carlo approaches based on equivalent formulations in terms of stochastic differential equations (SDEs) have become increasingly popular (see, *e.g.*, Florinski and Pogorelov, 2009; Effenberger et al., 2012; Kopp et al., 2012; Zhao et al., 2014; Boschini et al., 2019; Moloto et al., 2019; Vogt et al., 2020). Using this approach, the problem is reduced to finding a solution of the stochastic integral of a set of ordinary differential equations instead of the integral of a partial derivative differential equation. The use of an SDE-based numerical scheme leads to numerous advantages regarding other numerical methods. As clearly pointed out by Strauss and Effenberger (2017) these can be summarized as (i) unconditional stability, although this does not necessarily imply numerical accuracy, (ii) the method can handle large gradients, (iii) it allows to save computational memory, and, finally, (iv) every stochastic trajectory is independent of the others, which makes the problem ideally suited for parallel computation (see Strauss and Effenberger, 2017, for a complete overview of the use of SDE in particle transport problem in heliosphere). This last feature has fostered the adoption of graphics processing units (GPUs), whose parallel architecture allows the integration of large ensembles of trajectories simultaneously, thus drastically reducing computing time and achieving performance levels unattainable with traditional CPU-based approaches (see, *e.g.*, Dunzlaff et al., 2015; Vogt et al., 2020; Solanik et al., 2022; Solanik et al., 2023).

Nowadays it is possible to find several codes that apply this approach to solving the PTE but just a few of them implement GPU in their algorithms: HelMod-4/CUDA (Boschini et al., 2024) a closed source GPU implementation of HelMod-4 model (Boschini et al., 2019), Geliosphere (Solanik et al., 2023) an open source fork of SOLARPROP (Kappl, 2016) code, SDEMMA (Qin and Shen, 2017) a closed source code solving a time-dependent 3D solution of the PTE, and some ad-hoc unnamed models (see, *e.g.*, Strauss et al., 2011b; Dunzlaff et al., 2015; Moloto et al., 2019). All these codes were developed with the intention of exploring and expanding the physical model. In this paper, we change the point of view and study how to optimize the performance of such an approach, reaching as close as possible to the technical limits of present GPU hardware. In fact, despite the good performances of the previously mentioned codes, heavy-computational parameter searches still require a considerable effort that can be supported by only national HPC centers (see, *e.g.*, discussion in Section 3.2 in Della Torre et al., 2025). COSMICA code, presented in Bacciu et al. (2026), is an open source code solving the 3D-PTE using SDE-Monte Carlo approach on (multi-)GPUs. The code is written in CUDA/C++ in order to implement the fastest GPU framework to date. This work follows the one presented in Bacciu et al. (2026), validating the code with respect to a benchmark model. In order to have a benchmark, the physical model implemented in this work is based on HelMod-4/CUDA (Boschini et al., 2024), which demonstrated to reproduce experimental data both at Earth orbit, outside ecliptic plane, and at several solar distances; moreover, along with SDEMMA, in one of the only models that, to date, can reproduce high Z cosmic ions up to $Z = 28$ (Shen et al., 2019). In addition, the code performance was benchmarked against Geliosphere (Solanik et al., 2023), which shows a simplified model with respect HelMod-4/CUDA and with a numerical implementation designed to run both on CPU and GPU.

This Paper is organized as follows: Section 2 outlines the theoretical framework of the Parker Transport Equation and the SDE Monte-Carlo approach; Section 3 describes the COSMICA model utilized for validation; Section 4 details the results of the code's validation and benchmark against the reference models; Section 5 elucidate the possibility to study the distribution of the stochastic paths; and finally Section 6 summarizes the conclusions and discusses future work.

2. Parker transport equation

The transport equation for cosmic rays in the heliosphere was initially derived by Parker (1965) who demonstrated that – in the framework of statistical physics – the random walk of the cosmic ray particles is a Markov process, describable by a Fokker–Planck equation (see, *e.g.*, Potgieter, 1998; Leroy and Rancoita, 2011, and references therein)

The PTE was originally described in terms of the particle density (U) for unit space and energy (Bobik et al., 2012, 2016), which highlights the physical dependence of solar modulation by kinetic energy (hereafter labeled as T). On the other hand, particle propagation in the heliosphere is related to magnetic interaction between the charged particle and the magnetized plasma of the interplanetary medium, thus, particle rigidity ($R = \frac{pc}{Ze}$ where p is particle momentum, c is light speed and Ze is the particle charge) represents a more natural unit in which to explore process description. For this reason, several authors prefer to describe the modulation of cosmic rays by means of the so-called omnidirectional distribution function f (see, *e.g.*, Strauss and Effenberger, 2017; Engelbrecht et al., 2022):

$$\frac{\partial f}{\partial t} = \nabla \cdot \left(\mathbf{K^S} \cdot \nabla f\right) - \left(\mathbf{v_d} + \mathbf{v_{sw}}\right) \cdot \nabla f + \frac{R}{3} \nabla \cdot \mathbf{v_{sw}} \frac{\partial f}{\partial R} - Lf + S \tag{1}$$

where f is the average over all directions of the number of particles in the infinitesimal space volume element at time t and per unit of momentum; $\mathbf{K}$ is the diffusion matrix, which describes the permeability of the heliospheric medium regarding CR particles diffusion, and is usually divided in a symmetric term ($\mathbf{K^S}$) describing the GCR diffusion – through the term $\nabla \cdot \left(\mathbf{K^S} \cdot \nabla f\right)$ –, and an antisymmetric term ($\mathbf{K^A}$) describing particle drifts (described in Eq. (1) as $\mathbf{v_d} \cdot \nabla f$); $\mathbf{v_d} = \nabla \cdot \mathbf{K^A}$ is the magnetic drift velocity, which includes cosmic ray drift along the Heliospheric Current sheet (HCS), and drift due to gradients and curvature in the 3D heliospheric magnetic field; $\mathbf{v_{sw}}$ denotes the outward solar wind speed, which is included in the PTE as a convective contribution to the particle transport ($\mathbf{v_{sw}} \cdot \nabla f$) and describes the GCR adiabatic rigidity changes ($\frac{R}{3} \nabla \cdot \mathbf{v_{sw}} \frac{\partial f}{\partial R}$); finally, in this more extended formulation, S represents any particle source that may be present in the domain where PTE is solved,[1] and L are the catastrophic losses, like particle decays or absorptions (see, *e.g.*, example in Strauss and Effenberger, 2017, and reference there in). U and f are related to each other by means of the differential intensity J (see, *e.g.* Bobik et al., 2016):

$$J = \frac{\beta c U}{4\pi} = p^2 f \tag{2}$$

This quantity, expressed in $[m^2\ s\ sr\ GV]^{-1}$, is also the physical quantity that can measured by space spectrometers, *i.e.*, AMS–02 (Aguilar et al., 2021, and reference there in) and PAMELA (Martucci et al., 2018, and reference there in). Hereafter, we refer to J as modulated GCR spectra, while the LIS is labeled as J_{LIS}. It is important to remark that space spectrometers can measure J per unit of particle rigidity, while other space detector technologies (like, *e.g.*, calorimeter-based detectors) measure J per unit of kinetic energy per nucleon (expressed in $[m^2\ s\ sr\ GeV/n]^{-1}$). In this paper, $J(R)$ refers to the spectra computed

[1] For example, Jovian magnetosphere is known to be a source of low energy electron, thus it could be included into the PTE as a point like source of CR as described in, *e.g.*, Nndanganeni and Potgieter (2018) and Vogt et al. (2018, 2020, 2022) and references therein.

per unit of rigidity, while with $J(T)$ we refer to the spectra computed per unit of kinetic energy per nucleon.[2]

2.1. The benchmark model

For the purpose of this project, which is focused on studying the computational implementation of the SDE solver, leaving for successive papers a deeper focus on exploring the features of the physical model, we based our code on the HelMod-4/CUDA model described in Boschini et al. (2018b, 2019) that in the last years was specialized to (successfully) reproduce the long-term solar modulation (Bobik et al., 2012; Della Torre et al., 2012; Boschini et al., 2018b, 2019; Bartocci et al., 2020; Rankin et al., 2022), with an accuracy level comparable to the actual experimental uncertainties (*i.e.*, a few percent for AMS-02 time-integrated spectra). The code, used in combination with GALPROP (Boschini et al., 2017), has been used to infer the LIS for particles with the atomic number up to $Z = 28$ (Boschini et al., 2018a,c, 2020b,a), allowing to highlight fine structures in GCR observed spectra (Boschini et al., 2021, 2022a,b). Finally, it was demonstrated that the model is also suitable for assessing the potential radiation risk in the space environment (see, *e.g.*, Boschini et al., 2022c; Liu et al., 2024). Here we recall only the general structure of the model, while a detailed description can be found in Boschini et al. (2018b, 2019, 2024, and references therein). K^S is defined in the reference frame of the magnetic field line where the tensor is simplified to a diagonal matrix with non-zero values on the diagonal, which are referred to as the diffusion coefficient parallel to the HMF ($K_\parallel$), and to the two diffusion coefficients perpendicular to the HMF line ($K_{\perp,\theta}$ and $K_{\perp,\phi}$); $K_\parallel$ is defined by the linear rigidity dependence (Boschini et al., 2017):

$$K_\parallel = \frac{\beta}{3} K_0 \left(\frac{R}{1\ \mathrm{GV}} + g_{\mathrm{low}} \right) \left(r_c + \frac{r}{1\ \mathrm{AU}} \right) \tag{3}$$

where K_0, called the *diffusion parameter*, is an important parameter for the model since it allows setting the absolute scale of the solar modulation intensity; it is evaluated with the procedure described in Boschini et al. (2018b, and reference therein). g_{low} and r_c, instead, are data-tuned time-dependent free parameters allowing the detailed modeling of specific features of the modulated spectra and radial gradient measured by Voyager probes (Boschini et al., 2018b, 2019). $K_{\perp,\theta}$ and $K_{\perp,\phi}$ are supposed to be proportional to $K_\parallel$ through a proportional parameter tuned on the latitudinal gradient measured outside the ecliptic plane (Bobik et al., 2013; Boschini et al., 2018b, 2019). When included in Eq. (1), a change of reference system to the heliocentric inertial system is applied to K^S as described in Burger et al. (2008). The drift model implemented includes cosmic ray drift along the Heliospheric Current Sheet (HCS) and drift due to gradients and curvature in the 3D heliospheric magnetic field (Jokipii et al., 1977; Jokipii and Thomas, 1981; Hattingh and Burger, 1995). The code includes the description originally developed by Potgieter and Moraal (1985); it was refined using Parker's magnetic field (Jokipii and Kóta, 1989) with polar corrections as reported in Bobik et al. (2013) (see also Raath et al., 2016, for a discussion about modified Parker's magnetic field). Finally, drift velocity suppression factors were introduced to reduce the global effect of CR drift in the heliosphere due to the presence of turbulence in the interplanetary medium (see discussion in Ferreira and Potgieter, 2004; Bobik et al., 2013; Engelbrecht et al., 2017; Boschini et al., 2019). Although the HelMod-4/CUDA model relies on several free parameters, a procedure of iterative tuning involving the code GALPROP for LIS estimation and the most recent proton measurements of AMS–02 and PAMELA allowed the HelMod-4/CUDA developers to constrain most of the free parameters and to find correlations with observational quantities for those parameters that evolve with time (Bobik et al., 2012; Boschini et al., 2017, 2019, 2024, and reference therein). In particular, the physical parameters that must be provided with the simulation are (a) the values of Smoothed Sunspot Numbers (SSN, Royal Observatory of Belgium, 2025), (b) the Neutron monitor counting rates (NMCR, database, 2025), (c) the solar wind speed ($V_{sw,\oplus}$), (d) the magnetic field amplitude ($B_\oplus$), (e) the tilt angle (α_t) of HCS (the "line-of-sight" model Hoeksema, 1995) (f) the magnetic field polarity, and, finally, (g) the position of the TS and HP computed with the formulas in Boschini et al. (2019). $V_{sw,\oplus}$ and $B_\oplus$ are evaluated at Earth's orbit and provided by NASA/GSFC's Space Physics Data Facility's OMNIWeb service (King and Papitashvili, 2020). α_t and the magnetic field polarity are provided from the Wilcox Solar Observatory Polar Field Observations (Observatory, 1995).

The geometrical shape of the heliosphere is modeled with two concentric quasi-spheres, the inner heliosphere and the heliosheath (Langner and Potgieter, 2004). The inner heliosphere and the heliosheath are divided by the termination shock (TS) while the heliopause (HP) marks the external boundary of the heliosphere. An asymmetry in the direction of the interstellar medium (ISM) flow is introduced to account for the latitudinal variation of the ISM ram pressure component of the total pressure on the HP surface (Boschini et al., 2019). Since the solar disturbances travel across the heliosphere within the solar wind, it is reasonable to suppose that GCR, while traveling through the heliosphere, experienced different solar activity-induced disturbances. For this reason, the inner heliosphere is divided into 15 effective shells, each one with its own observational quantities, numbered from the heliosphere center ($n = 0$) to the external boundary ($n = 14$), and where the n-shell refers to a time shift equal to n Carrington rotations[3] regarding the simulated time at Earth orbit (Bobik et al., 2012). The heliosheath, instead, is treated as a single separated region where the propagation is one-dimensional (Boschini et al., 2019).

For comparison purpose, in Section 4, we also present the execution time performance with the code Geliosphere (the complete description of the code can be found in Solanik et al., 2023). The *out-of-the-box* model of Geosphere implemented by Solanik et al. is simpler with respect to the one described in this section, since it does not include propagation in the heliosheat as well as native support for separate isotope contribution to solar modulation. Geliosphere demonstrated its capability to reproduce latitudinal gradients observed by Ulysses mission, while, as stated by authors, *shows no satisfactory agreement with AMS-02* (see section 2.3 in Solanik et al., 2023).

2.2. SDE Monte-Carlo approach

Fokker–Planck-type equations (sometimes referred to as Kolmogorov equations) have the interesting property that they can be rewritten in a fully equivalent set of stochastic differential equations (SDE) in the form (Øksendal, 2010; Freidlin, 1985):

$$dy_i(s) = A_i(y,s)ds + \sum_j B_{i,j}(y,s)dW_j(s) \tag{4}$$

in the SDE formalism, ds represent the backward in time step; $A_i(y,s)$ is the advective term that contains all deterministic processes like convection and particle drift; $\sum_j B_{i,j}(y,s)dW_j(s)$ is the diffusive term that describes all stochastic processes like particle diffusion and shock re-acceleration, in this term dW indicates the increment due to a *standard Wiener process* (see, *e.g.*, Appendix A of Zhang, 1999 and Section 2 of Higham, 2001), a time stationary stochastic Lévy process where the time increments have a Normal distribution with a mean of zero (*i.e.* a Gaussian distribution) and a variance of dt (see introduction of Gardiner, 2009). The procedure to convert PTE into SDE is described

[2] To convert from one formulation to the other we apply the conversion formula $J(T) = J(R)\frac{dT}{dR} = \frac{J(R)}{\beta}$ where β is the velocity of the particle in units of light speed, a quantity that can be easily computed once known the kinetic energy per nucleon. Please note that Eq. (2) is valid only with $J(T)$.

[3] A Carrington rotation, ~27.27days, corresponds to a Sun rotation on its axis at 26° of solar latitude as seen by an observer on the Earth.

by many authors (Gardiner, 1985; Zhang, 1999; Strauss et al., 2011a; Kopp et al., 2012; Bobik et al., 2016; Strauss and Effenberger, 2017; Boschini et al., 2018b) and can be summarized as rewriting Eq. (1) in the form:

$$\frac{\partial f}{\partial s} = \sum_i A_i(s,y)\frac{\partial f}{\partial y_i} + \frac{1}{2}\sum_{i,j} D_{i,j}(s,y)\frac{\partial^2 f}{\partial y_i \partial y_j} - Lf + S \tag{5}$$

$\mathbf{D} = \mathbf{B}\mathbf{B}^{\mathbf{T}}$ where $\mathbf{A}$ and $\mathbf{B}$ are the same as Eq. (4) and can be found in Appendix A of Boschini et al. (2018b). One may notice the L and S terms are not present in Eq. (4), this is due to the fact that, indeed, the presence or absence of these terms does not affect the stochastic path directly but are accounted as a probabilistic weight carried out by the *quasi-particle* event. As we see in the following paragraph, *quasi-particle* events have a statistical weight that may increase or decrease along the stochastic path according to the presence of processes like the ones described by L and S terms.

The Monte Carlo method of assessing the modulated spectra consists of evolving a collection of points in the phase space $(\mathbf{x}, R, s)$, backward in time[4] and according to the discrete version of Eq. (4) using the Euler-Maruyana scheme (see, *e.g.*, Ref. Kroese et al. (2011), Section 5.6.1), from the evaluation point (*i.e.*, the point $\mathbf{x}_0, R_0, s_0$ where the modulated flux should be evaluated) up to the external boundary of the heliosphere. These evolving elements are hereafter referred to as *quasi-particle* objects since their evolution mimics the paths that GCR particles may cover, but their paths are not real trajectories; in fact, as pointed out in Strauss and Effenberger (2017) and by Boschini et al. (2024), integrating Eq. (4) for a single quasi-particle bears no significance: each computed trajectory is a probabilistic flight that contributes to defining a quasi-Green function representing the probability that a particle, observed at a given detection point and characterized by a certain particle rigidity R_0, entered the heliosphere (*i.e.*, before the modulation process starts) with initial particle rigidity R. To consider losses and sources the *quasi-particle* object may encounter during its passage through the physical domain, we have to introduce two additional quantities: the path weight, α, with initial value $\alpha_0 = 1$, and the path amplitude, W, with initial value $W = 0$. The path weight changes at each j_{th} step during the propagation (from generation $j = 0$ to registration $j = f$) by a factor $\exp(-L\Delta s)$ leading to (see, Equation 22 in Kopp et al., 2012):

$$\alpha_j = \alpha_{j-1} \cdot e^{-L_j \Delta s} = \exp\left(-\sum_{k=0}^{j} L_k \cdot \Delta s\right), \tag{6}$$

where the index $j-1$ refers to the previous time step. If the *quasi-particle* object encounters a source defined by the term S, the path amplitude is enhanced by the source strength (S_j) weighted with the current path weight (α_j) (see, Equation 23 in Kopp et al., 2012):

$$W_j = W_{j-1} + S_j \cdot \alpha_j \tag{7}$$

When the boundary of the simulation is reached, the time integration stops (path weight and path amplitude computed up to this step are now marked with a subscript $_f$). The total path amplitude associate with the *quasi-particle* object is the summation of the integrated value of (W_f *i.e.*, the amplitude due to source encountered during the propagation), and the final path weight multiplied by the boundary weight, *e.g.*, the LIS (see, Equation 24 in Kopp et al., 2012):

$$W_f = W_f + f_0 \cdot \alpha_f \tag{8}$$

where f_0, in this paper, is the value of f (defined in Eq. (2)) at the exit value of Rigidity. The modulated spectrum, computed with N Monte Carlo trajectories, is then evaluated as,

$$f(\mathbf{x}_0, R_0, s_0) = \frac{1}{N}\sum_{p=0}^{N} W_f \tag{9}$$

This represent the most general expression for evaluating the Monte Carlo solution with SDE method while including point-like CR source term or secondary CR production process in the interplanetary medium. In the physical model solved in this paper, we do not account for any source or loss term; thus, the corresponding L and S terms in Eq. (5) are set to zero,[5] which reduces $W_f = f_0 = \frac{J_{LIS}}{p^2} = \frac{J_{LIS}}{R^2}\left(\frac{c}{Ze}\right)^2$ when applyng Eq. (2). The modulated spectra are then obtained by applying the following formula:

$$J(\mathbf{x}_0, R_0, s_0) = \frac{\beta_0 R_0}{N}\sum_{p=0}^{N}\frac{J_{LIS}(T_p)}{R_p^2} \tag{10}$$

where p is the index identifying each *quasi-particle* object, R_p and T_p are the values of the *quasi-particle* object rigidity and kinetic energy per nucleon at the end of the stochastic trajectory, $J_{LIS}(T_p)$ is the LIS spectra evaluated at T_p, and β_0 is the conversion factor from $J(T_0)$ to $J(R_0)$ as discussed in Section 2.

It is interesting to note that Eq. (10) can be approximated by evaluating the distribution function of R_p, *i.e.* $G(R_0|R)$ which describes the normalized probability that a *quasi-particle* object generated with initial rigidity R_0, when reaching the external boundary, has rigidity R (Zhang, 1999).

$$J(\mathbf{x}_0, R_0, s_0) \approx \beta_0 R_0 \int_{R_0}^{\infty}\frac{J_{LIS}(R)}{\beta(R)R^2}\cdot G(R_0|R)dR \tag{11}$$

$$\approx \beta_0 R_0 \sum_i \frac{J_{LIS}(R_i)}{\beta(R_i)R_i^2}\cdot G_{R_0}(R_i)\Delta R_i \tag{12}$$

where G_{R_0} is the histogram with bin amplitude ΔR_i and bin center R_i mapping the function $G(R_0|R)$. This approach has the advantage of restricting the amount of information that must be stored in memory during the computation, since, instead of recording all particles, it records the histogram of the distribution function. Moreover, J_{LIS} can be applied in a post-simulation phase, and any modification to the LIS prediction (for example, while studying specific features of the spectra) can be applied in post-processing without rerunning the whole simulation.

3. The COSMICA numerical solver

We developed COSMICA as a numerical solver for Eqs. (4) in the case of the model presented in Section 2.1. COSMICA is implemented in CUDA (version $\geqslant$ 12.4) and C++20 for NVIDIA GPU architectures. The code is designed to make the simulation process highly parallelizable and efficient on modern High Performance Computing (HPC) systems. Each trajectory is assigned to a dedicated GPU thread, and particle-specific data and constants are carefully allocated across different GPU memory types according to their access patterns, maximizing computational throughput and resource efficiency. During propagation, each trajectory is advanced step by step using SDE integration until the stochastic path exits the simulation domain, *i.e. quasi-particles* reaches the HP. Results are stored in block-level histograms, reconstructing G_{R_0} in Eq. (12), with atomic operations to avoid conflicts and later transferred to the host. In multi-GPU setups, COSMICA automatically partitions the workload, allowing independent execution across devices without explicit synchronization. The host then merges the outputs into global histograms. COSMICA was designed to maximize the GPU

[4] It is worth mentioning that there also exists an equivalent forward-in-time approach, described in Bobik et al. (2016), which is not considered here since, in the framework of reproducing measured point like observation in the heliosphere, it shows lower performance in terms of computational time required to compute the solution.

[5] This is true because in this case the PTE is solved against rigidity; when solved against kinetic energy, the rewriting of PTE in the form of Eq. (5) leads to a non zero L term not directly connected to a real physical production/loss process that must be accounted for when evaluating the path weight.

Table 1
Simulated time intervals along with the corresponding solar activity and HMF polarity.

CR number	Start–End date	Solar activity	HMF polarity
2117	Nov. 16–Dec. 13, 2011	Solar minimum	Negative
2155	Sep. 17–Oct. 15, 2014	Solar maximum	Undefined
2168	Sep. 7–Oct. 4, 2015	Medium descendant	Positive
2181	Aug. 27–Sep. 23, 2016	Medium descendant	Positive
2192	Jun. 23–Jul. 20, 2017	Medium descendant	Positive
2209	Sep. 29–Oct. 26, 2018	Solar minimum	Positive

occupancy and, thus, push the computational effort to its limits, reducing at most any computational inefficiencies. More details on how the numerical solver is implemented were presented in Bacciu et al. (2026). The code has been released as open source under the GPLv3 license and is accessible through the project repository (Bacciu et al., 2025).

4. Computational performance assessment

Performances of COSMICA were evaluated both independently and compared to the benchmark model presented in Section 2.1. We performed principally two kinds of benchmark studies: during the benchmark test (A), we varied the number of *quasi-particles* realizations within the set $\{2^n \mid 9 \leqslant n \leqslant 16\}$ for a set of defined heliospheric parameters; during benchmark test (B), with a fixed number of *quasi-particles* realizations, we varied the values of a specific *dynamic parameter* (see description in Bacciu et al., 2026) within the set $\{2^n \mid 0 \leqslant n \leqslant 7\}$. Heliospheric parameters are taken to be representative of a single Carrington rotation, spanning 23 bins from 1 to 11 GV mapping the ones used for the latest proton measurements provided by AMS–02 (Aguilar et al., 2021), and evaluating the differential intensity of proton plus deuteron (*i.e.* hydrogen nuclei GCR usually referred to as simply *proton GCR*) measurements. Since performance increases with increasing the particle rigidity, higher bins were not considered in this work.

The simulated heliospheric parameter sets cover 6 different solar activity scenarios, as detailed in Table 1. We repeat all simulation tests 6 times with independent random seeds; this is to ensure statistical robustness. Multi-GPU systems configured with 2, 3, and 4 NVIDIA A100 GPUs were also tested. The legacy HelMod-4/CUDA simulator was used for benchmarking our results following the same protocol as described above.

4.1. Comparison with previous version

A primary objective of COSMICA is to enable the rapid execution of large-scale simulations. The majority of development decisions described Bacciu et al. (2026) were driven by this goal. Fig. 1a-b illustrates the speedup achieved by COSMICA compared to HelMod-4/CUDA when executed on a single NVIDIA A100 GPU.

As shown on the left side of the figure, COSMICA achieves a speedup exceeding 100× for smaller workloads. This substantial improvement is primarily attributed to enhanced particle ordering and dispatch strategies, which allow the GPU to reach saturation more rapidly and thereby maximize performance at an earlier stage. As the number of *quasi-particles* increases, the speedup stabilizes at approximately 12×, corresponding to conditions in which both COSMICA and HelMod-4/CUDA fully exploit the available computational resources. In fact, the onset of computational saturation is even more apparent in Fig. 1a, on the left panel. This transition is marked by the point at which the growth of execution time shifts from sub-linear to linear with respect to the number of *quasi-particles*. For HelMod-4/CUDA, this occurs at approximately 32 768 *quasi-particles*, whereas for COSMICA the transition is observed much earlier, at around 4096 *quasi-particles*.

Fig. 1c–d describes the actual runtimes (execution times) corresponding to the speedup results discussed above. A single simulation involving 4096 particles – which yields an error of approximately 1% – requires only about 10 s with COSMICA, in contrast to nearly 100 s with HelMod-4/CUDA.

The right panels of Fig. 1 illustrate both the speedup (1b) and execution time (1d) as functions of the number of tested dynamic parameters. It is evident that the speedup rapidly reaches a plateau exceeding 100×. This remarkable improvement is primarily attributable to the scheduling strategy adopted in COSMICA, wherein multiple parametrizations are executed concurrently within a single run. In contrast, the legacy HelMod-4/CUDA required separate sequential simulations for each parameterization, resulting in significantly increased computational time.

As an exhaustive example, a simulation involving numerous parametrizations that would previously have required approximately one month to complete using HelMod-4/CUDA code can now be executed in just over 7 h using COSMICA.

We also compared the performance improvement achieved with multi-GPU setups.

Panel (a) of Fig. 2 shows that the speedup is maximal when utilizing a single GPU. This phenomenon is analogous to the one described previously, and occurs because a single GPU reaches saturation with fewer particles, thereby achieving its peak performance more rapidly. As the particle count increases, all GPUs eventually become saturated – specifically beyond 32 768 *quasi-particles*– at which point the speedup plateaus.

In panel (b), a similar trend is observed for smaller numbers of parameter values. However, beginning with eight parameter values, there is a noticeable inversion in the trend: even four GPUs reach saturation, allowing the advantages of improved scheduling to become apparent. In this regime, the speedup continues to increase with the number of GPUs employed, reaching as high as 120× with four GPUs. Finally, panels (c)–(d) show the raw runtimes from which the speedups are computed. Together, they show that, once saturation is reached, COSMICA exhibits linear strong scaling – duplicating the number GPUs halves the runtime – and constant weak scaling, where doubling both the number of GPUs and the number of particles results in an unchanged runtime.

Similar analysis of the execution time was performed comparing COSMICA with Geliosphere (Solanik et al., 2023). The latter model has few differences with respect to the physical model described in Section 2.1, which is implemented as default version of COSMICA presented in this manuscript. For this reason, to ensure a fair comparison between the two, we tested three modifications to the COSMICA implementation. The first modification, *No Heliosheat*, removes the heliosheat from the model. In Geliosphere, particles exit the heliosphere when they arrive at the termination shock. With this modification, also in COSMICA the propagation is stopped once the termination shock is reached. The second modification is *Modified Physics*. This is meant to mitigate the differences in the constant heliosphere and propagation characteristics between the two models. With this modification, we update COSMICA to use $\frac{K_\perp}{K_\parallel} = 0.2$, $\delta_m = 8.7 \times 10^{-5}$, and no polar enhancement of $K_\perp$, as in Geliosphere. The third modification *Fixed Timestep*. In COSMICA, a dynamic timestep of $dt \in [0.01, 50.0]$ s is used, but with this modification, COSMICA adopts the same fixed timestep as Geliosphere ($dt = 5.0$ s). We tested Geliosphere, the default COSMICA version, and all combinations of the modifications described above over two Carrington rotations using the parameters from Table 2. In line with the Geliosphere implementation, for all COSMICA benchmarks in this comparison, the entire heliosphere was treated as a single zone with homogeneous parameters.

Fig. 3 shows the execution time comparison for different numbers of total simulated *quasi-particles* with AMS-02 rigidity binning. All benchmarks were ran on an NVIDIA A40 GPU. The Figure clearly shows that the presence of heliosheat impacts computational time, increasing it by a factor of approximately 2. The largest performance difference arises from using a dynamic time step instead of a fixed time step. We find that COSMICA outperforms Geliosphere in most of the comparisons

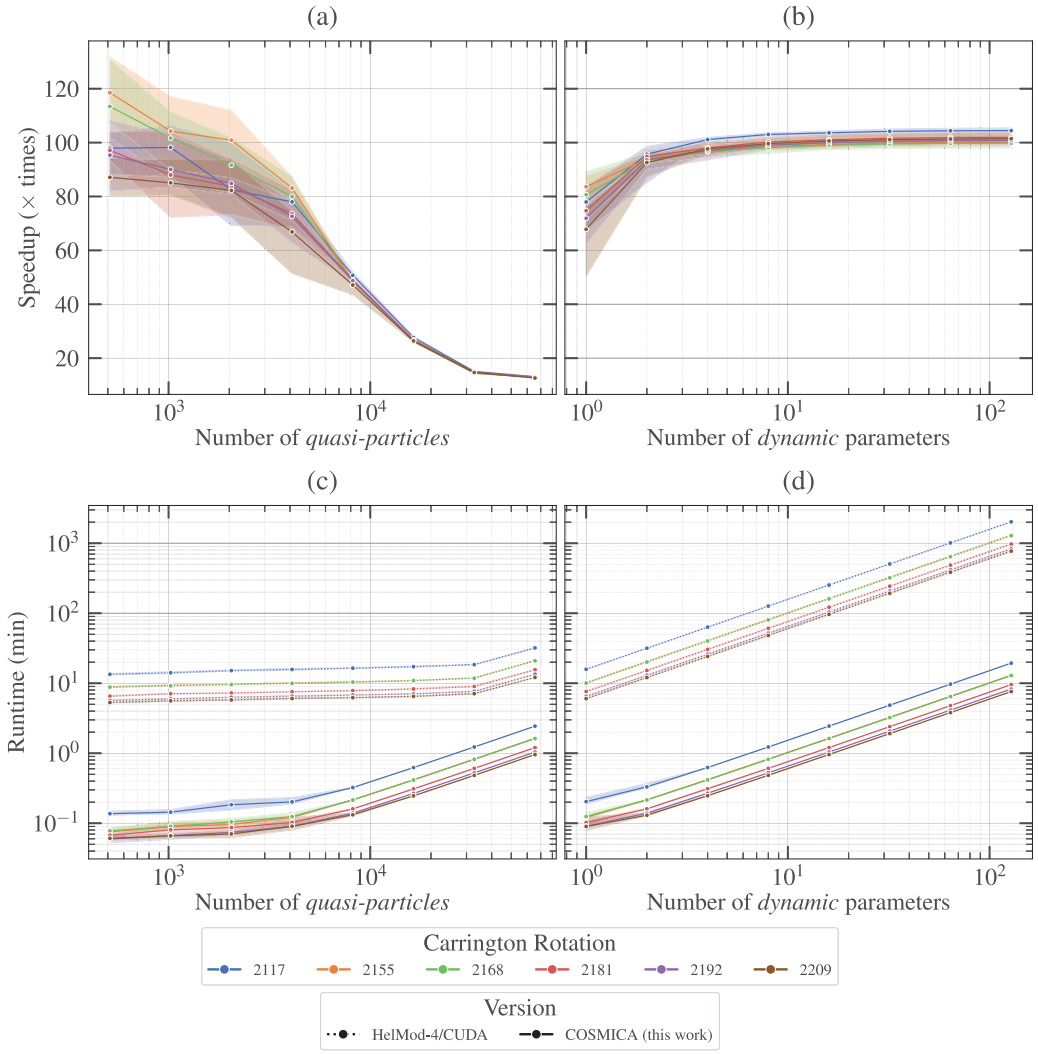

Fig. 1. Scaling analysis of the COSMICA multi-GPU implementation versus HelMod-4/CUDA for proton + deuteron simulations (23 bins, 1–11 GV) across different GPU architectures and simulation periods.
(a) Speedup as a function of *quasi-particle* count for different periods.
(b) Speedup as a function of parameter count (K_0) for different periods.
(c) Runtime as a function of *quasi-particle* count for different periods.
(d) Runtime as a function of parameter count (K_0) for different periods.
All results are shown for different simulation periods, with shaded areas indicating the 95% percentile interval.

presented, losing in performance only when both heliosheat particle propagation and a fixed time step are included. The COSMICA model is more complex, as it performs 3D propagation instead of 2D, and is designed to support multiple zones, parametrizations, and isotopes within the same simulation. These design choices impact execution time, as supporting multiple configurations requires considerably more memory accesses and registers. Despite this, thanks to the accurate code design presented in Bacciu et al. (2026) – focused on ensuring best as possible GPU performances – in all our tests the default COSMICA version achieves runtimes around an order of magnitude faster than Geliosphere.

4.2. Consistency with previous version

To verify that the recent updates did not alter the underlying functionality of the code, we compared the output fluxes generated by both HelMod-4/CUDA and COSMICA using identical input configurations. This comparison was conducted across all test cases previously employed to assess the impact of varying the number of *quasi-particles*.

Table 2
Parameters used for the comparison benchmarks between COSMICA and Geliosphere.

Parameter	CR 2217	CR 2155
$V_{sw,Earth}$	400 km/s	400 km/s
Termination shock	Fixed at 100 AU	Fixed at 100 AU
Heliosheat	Absent	Absent
K_0	4.12008×10^{-5} AU^2/2	3.2568×10^{-5} AU^2/2
Tilt angle	55.8°	65.5°

This leads to a test suite encompassing 6 Carrington rotations, 8 distinct values for the number of *quasi-particles*, 23 rigidity values, and 6 random seed initializations, leading to a total of $6 \cdot 8 \cdot 23 \cdot 6 = 6624$ tests per version. With this setup, we computed the relative difference between the output fluxes of HelMod-4/CUDA and COSMICA as follows

$$d = \frac{x_H - x_C}{\left(\frac{x_H + x_C}{2}\right)} = 2 \cdot \frac{x_H - x_C}{x_H + x_C} \tag{13}$$

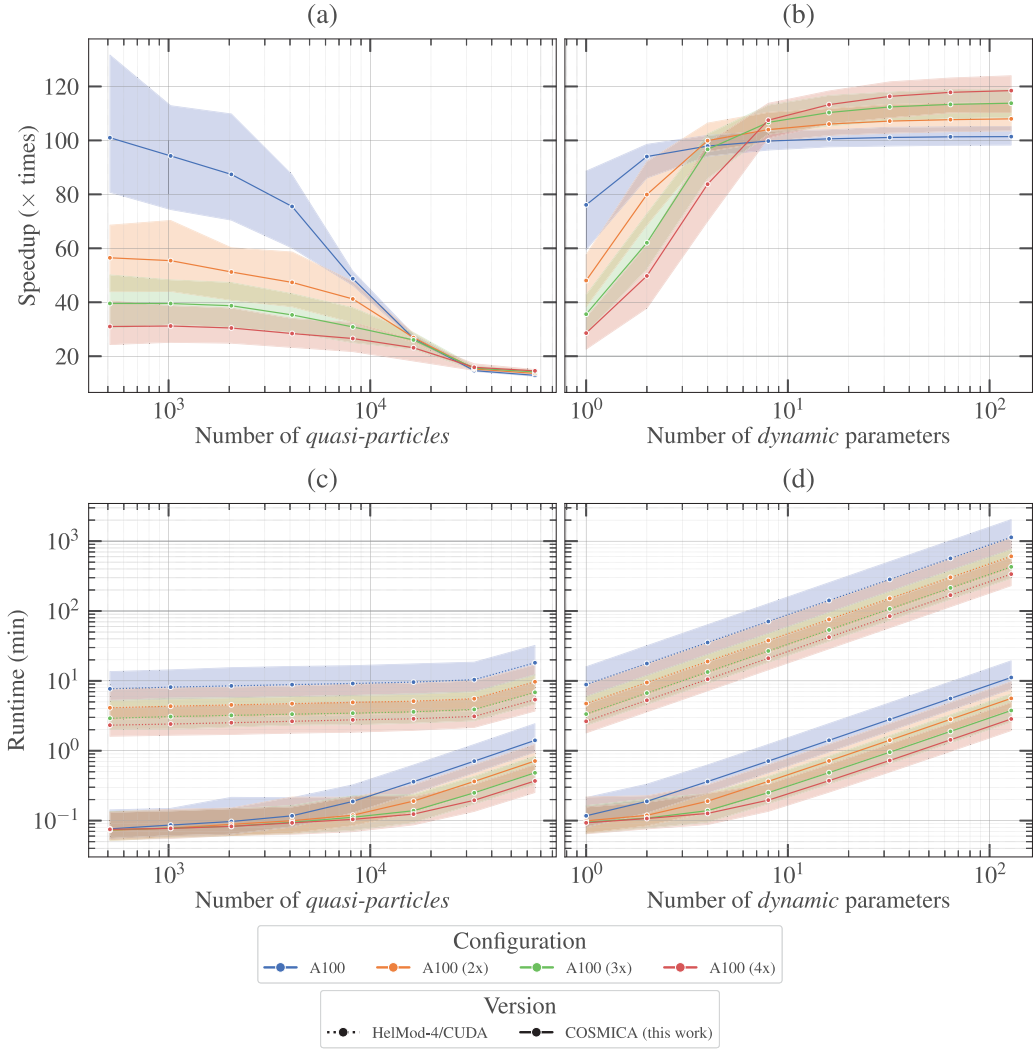

Fig. 2. Scaling analysis on multi-GPU configurations (1x, 2x, 3x, 4x A100s) for proton + deuteron simulations (23 bins, 1–11 GV) across different simulation periods.
(a) Speedup as a function of *quasi-particle* count for different number of GPUs.
(b) Speedup as a function of parameter count (K_0) for different number of GPUs.
(c) Runtime as a function of *quasi-particle* count for different number of GPUs.
(d) Runtime as a function of parameter count (K_0) for different number of GPUs.
All results are shown as aggregates over the 6 simulation periods from Table 1, with shaded areas indicating the 95% percentile interval.

where x_H is the output of HelMod-4/CUDA and x_C of COSMICA.

The difference d was computed and then averaged over all rigidities, Carrington rotations, and random seeds. This approach is justified because relative differences are directly comparable to each other and do not depend on the magnitude of the initial rigidity, thereby facilitating straightforward aggregation.

Row $\bar{D}$ in Table 3 reports the sample mean values of these relative differences, while row S^2_D presents the corresponding sample variances. For example, considering 4096 *quasi-particles*, the observed distribution is $-7.76 \cdot 10^{-4} \pm 6.60 \cdot 10^{-5}$, showing a mean value very close to zero and a small variance. This outcome suggests that the differences between the two simulations are centered around zero, as expected, but further justification for the magnitude of the variance is warranted.

Assuming that the outputs of both simulations are independent and drawn from the same normal distribution with fixed mean and small variance, $X_H, X_C \overset{\text{i.i.d.}}{\sim} \mathcal{N}(\mu, \sigma^2)$, we can express:

$$D = 2 \cdot \frac{X_H - X_C}{X_H + X_C} \tag{14}$$

In this context, x_H, x_C, and d represent all the individual realizations of the respective random variables X_H, X_C, and D. From the collected data, we can compute the sample mean ($\overline{X_H}$, $\overline{X_C}$, $\bar{D}$) and sample variance ($S^2_{X_H}$, $S^2_{X_C}$, S^2_D) for each quantity.

Given that Eq. (14) is a function of two random variables, we can derive its theoretical variance. To simplify this calculation, we introduce the practical assumption that $\mu \gg \sigma$, *i.e.*, the mean is much larger than the standard deviation. This allows us to approximate the denominator in Eq. (14) by 2μ, yielding the following expression for the variance of D:

$$\mathrm{Var}[D] = 2^2 \frac{\mathrm{Var}[X_H] + \mathrm{Var}[-X_C]}{(2\mu)^2} = 2\frac{\sigma^2}{\mu^2} \tag{15}$$

Although the exact values of μ and σ^2 are unknown, we can estimate them from the data using the sample mean and sample variance. This enables us to construct a statistical estimator for the variance of D, which can then be compared to the sample variance of D obtained from the simulations. If the estimated and observed variances are in close agreement, this supports the validity of our assumptions and provides strong evidence that the outputs of the two simulation codes

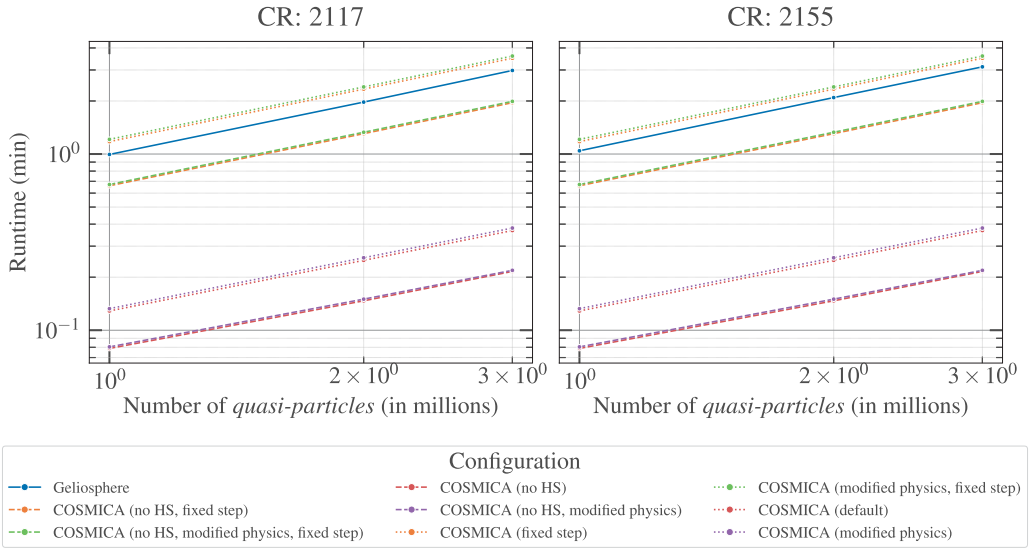

Fig. 3. Execution time comparison for different number of total simulated *quasi-particle* with AMS-02 rigidity binning. Geliosphere is reported as blue line. COSMICA runtime is evaluated for default (see Section 2.1) model or with parameter described in Table 2, with or without (no HS) heliosheat propagation, and with dynamic or fixed time step.

Table 3
Comparison of flux means, variances, and relative difference statistics for varying particle counts. The table presents the sample mean and sample variance for the flux and the relative difference, as well as three different estimates of the relative difference variance. These quantities are computed from the flux measurements of two models, X_H from HelMod-4/CUDA and X_C from COSMICA.

quasi-particles	512	1024	2048	4096	8192	16 384	32 768	65 536
$\overline{X_H}$	3.60e2	3.60e2	3.60e2	3.60e2	3.61e2	3.60e2	3.60e2	3.60e2
$\overline{X_C}$	3.61e2	3.60e2	3.61e2	3.61e2	3.60e2	3.61e2	3.61e2	3.61e2
$S^2_{X_H}$	1.26e2	6.18e1	3.17e1	1.61e1	8.94e0	4.32e0	1.95e0	9.92e−1
$S^2_{X_C}$	2.11e2	4.87e1	1.82e1	1.81e1	4.60e0	2.47e0	2.07e0	9.44e−1
$\overline{D}$	−1.71e−4	1.35e−4	−1.85e−3	−7.76e−4	−3.40e−5	−4.06e−4	−4.05e−4	−3.71e−4
S^2_D	5.30e−4	2.26e−4	1.09e−4	6.60e−5	3.10e−5	1.50e−5	7.00e−6	4.00e−6
$\widehat{\mathrm{Var}}_{X_H,X_C}[D]$	5.66e−4	2.38e−4	1.07e−4	6.90e−5	3.00e−5	1.40e−5	8.00e−6	4.00e−6
$\widehat{\mathrm{Var}}_{X_H}[D]$	5.01e−4	2.54e−4	1.23e−4	6.60e−5	3.40e−5	1.60e−5	8.00e−6	4.00e−6
$\widehat{\mathrm{Var}}_{X_C}[D]$	6.30e−4	2.22e−4	9.00e−5	7.30e−5	2.50e−5	1.20e−5	8.00e−6	4.00e−6

are identically distributed. The choice of an appropriate estimator for $\mathrm{Var}[D]$ is not straightforward; therefore, we considered three options:

$$\widehat{\mathrm{Var}}_{X_H}[D] = 2\frac{S^2_{X_H}}{\overline{X_H}^2} \tag{16}$$

$$\widehat{\mathrm{Var}}_{X_C}[D] = 2\frac{S^2_{X_C}}{\overline{X_C}^2} \tag{17}$$

$$\widehat{\mathrm{Var}}_{X_H,X_C}[D] = \frac{1}{2}\left(\widehat{\mathrm{Var}}_{X_H}[D] + \widehat{\mathrm{Var}}_{X_C}[D]\right) \tag{18}$$

Table 3 reports these estimated variances, averaged aggregated by the number of *quasi-particles*. It is evident that the estimated value is always very close to the measured one. This agreement indicates that the entire fluctuations in the distribution of the relative error are fully accounted for by the stochasticity inherent in the simulations, and not differences between HelMod-4/CUDA and COSMICA. Further confirmation is provided by Figs. 4–5, which shows a representative example of the overlapping fluxes together with the corresponding relative errors . This further confirms the statistical consistency of the two simulation pipelines, without any detectable systematic differences. Accordingly, all comparisons with experimental data are referenced to Boschini et al. (2024).

5. Analysis of the stochastic path

An interesting property of the SDE integration is the possibility to study the distribution of the stochastic paths. As already discussed, a single stochastic path is not informative, but the ensemble of many stochastic paths allows one to reconstruct the probabilistic properties of the particle transport through the medium. One example is the distribution of *last computed rigidity* that appears in Eq. (12). In this section, we show three other classes of distributions that can be inferred from COSMICA which provide additional information about the physical process: exit-point colatitude, propagation time, and resident time. The computed periods are reported in Table 1 which covers two periods of minimum solar activity with opposite HMF polarity, one period during solar maximum, and three intervals during the descending phase of solar activity during solar cycle 24. For the sake of clarity, we show only solar minimums and the solar maximum results, since the other periods show intermediate results with the same features as those presented.

5.1. Exit-point colatitude distribution

The stochastic path of *quasi-particles* objects ends when reaching the heliopause distance. The distribution of these *exit points* of the stochastic paths represents the probability that a particle entering the

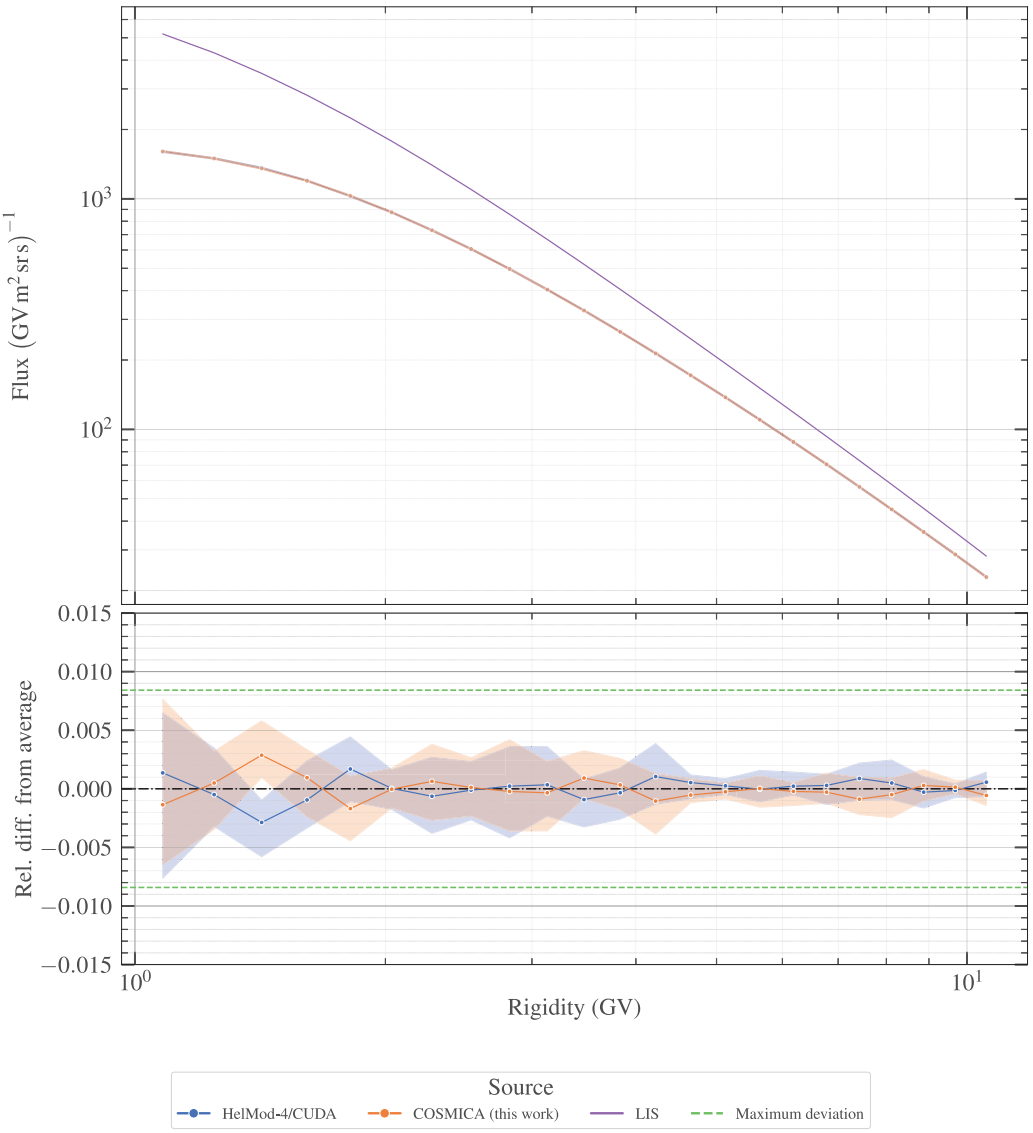

Fig. 4. Comparison between HelMod-4/CUDA and COSMICA over CR 2209 for proton + deuteron simulations (23 bins, 1–11 GV) with 8192 particles.
(Top) Output flux of the simulations, and LIS.
(Bottom) Relative difference between HelMod-4/CUDA and COSMICA with the average intensity including all realizations from both codes.
All results are shown as aggregates over 6 different random seeds, with shaded areas indicating the 95% percentile interval.

heliosphere from such a direction could reach the simulated initial position (the Earth in this work). In principle, since the boundary distribution of GCR is isotropic, one could expect a quasi-isotropic distribution of the *exit points*. As pointed out by many studies, the presence of magnetic drift in the PTE introduces a strong asymmetry (see, *e.g.*, Strauss et al., 2012; Tomassetti et al., 2025), limiting the capabilities for GCR to penetrate the heliosphere outside certain preferred directions. When HMF has positive polarity, positively charged particles entering the heliosphere from its polar region are more likely to reach the most inner parts than those entering from the equatorial region, where the HCS drift sums the solar wind outward flow with a net effect of increasing the advective outward transport (see, *e.g.*, Figure 1 in Dunzlaff et al., 2008). During periods with negative HMF polarity, drift velocity directions are inverted, causing particles reaching the Earth to be more likely to come from the equatorial boundary of the heliosphere (see, *e.g.*, Potgieter and Ferreira, 2001; Valdés-Galicia, 2005; Dunzlaff et al., 2008; Strauss et al., 2012; Moraal, 2014; Tomassetti et al., 2025). In Fig. 6 we show the exit colatitude (θ) of backward propagated *quasi-particles* with COSMICA. There, all the positive polarity periods exhibit two narrow peaks at the poles, with the same morphology. The only negative polarity period (CR2117) shows a distribution with a single peak in the equatorial region and a flattening in the polar region. This is a consequence of the preferential inward path along the neutral sheet and the outward drift at the poles (Dunzlaff et al., 2008). It is interesting to note that there is no difference when considering proton and deuteron GCRs, which have the same electric charge but double the mass. This is because the calculation was done for the same rigidity. Using these quantities, the difference in particle mass does not produce noticeable effects in the particle propagation. Thus, a similar distribution could be reasonably expected also for heavier ions and lighter charged particles.

As a final remark, the scenario described in this section should be inverted when considering negatively charged particles. This is because in determining the sign direction of the drift velocity component in the PTE, the relevant quantity is the sign product between HMF polarity

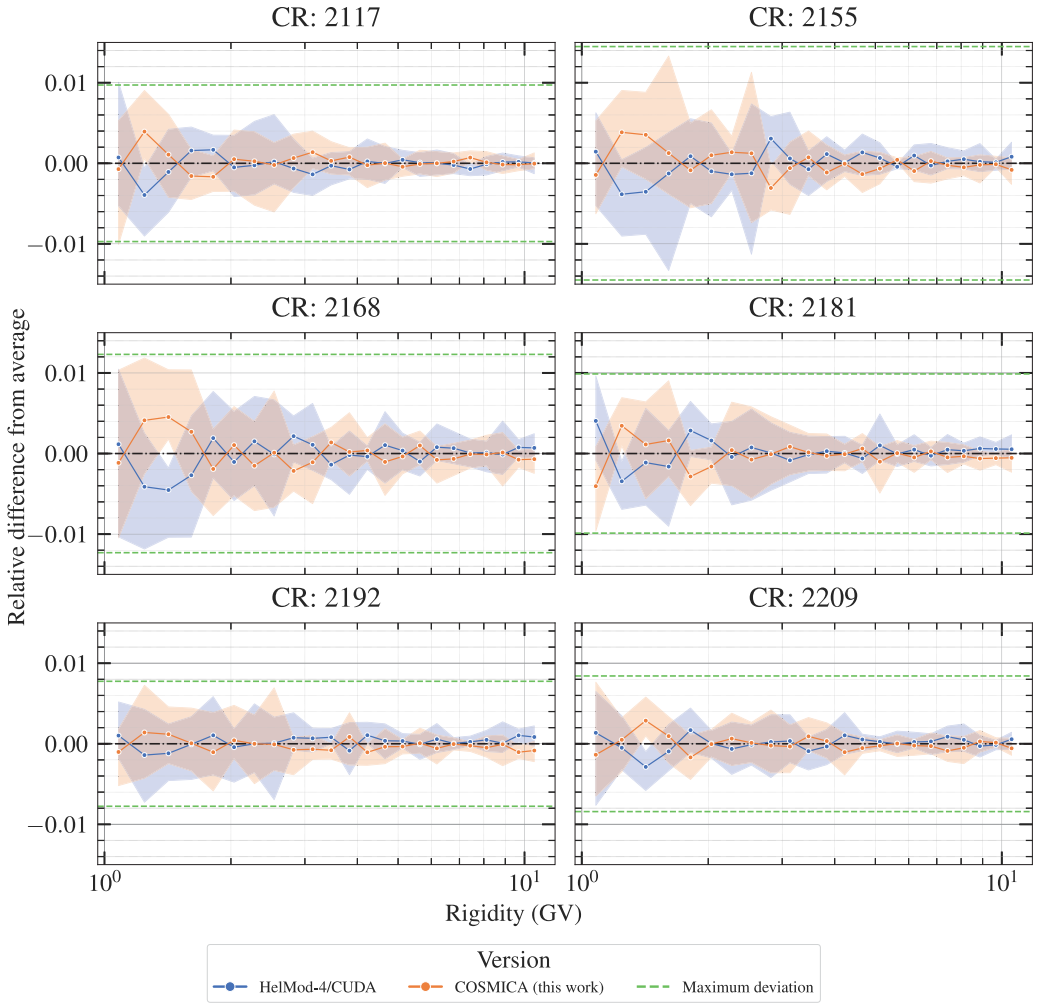

Fig. 5. Relative difference between HelMod-4/CUDA and COSMICA with the average intensity including all realizations from both codes and evaluated over the 6 simulation periods from Table 1, for proton + deuteron simulations (23 bins, 1–11 GV) with 8192 particles.
All results are shown as aggregates over 6 different random seeds, with shaded areas indicating the 95% percentile interval.

and particle charge. This asymmetry in the particle behavior is a well known effect that was observed in GCR and causes, for example, variation in the shape of positron fraction measured by PAMELA and AMS-02 (see, *e.g.*, Della Torre et al., 2012), different latitudinal gradients observed by the Ulysses probe (see, *e.g.*, Gieseler and Heber, 2016; Boschini et al., 2019, and reference there in), and different hysteresis figures when comparing particle and antiparticle flux (see, *e.g.*, Figure 3 in Aguilar et al., 2025).

5.2. Propagation and resident time

Another interesting quantity to be studied is the distribution of the duration of the propagation from the Earth to the external boundary. Since the rigidity loss (gain in backward-in-time) is modeled as a deterministic term in Eq. (4), the more the *quasi-particle* object resides in the heliosphere, the more rigidity it loses (gains in backward-in-time). In the actual model, the rigidity loss term is null in the heliosheath; thus, only the propagation time below the termination shock is relevant for the computation of the modulation intensity. In this context, the propagation in the heliosheath serves to estimate the fraction of reentrant particles (see, *e.g.*, Bobik et al., 2008) which contribute to increasing the propagation time below the termination shock and, thus, the intensity of the solar modulation. In Fig. 7 we report the propagation time of both protons and deuterons *quasi-particles*, divided by the resident time before and beyond the termination shock (*i.e.*, inside the inner heliosphere and in the heliosheath). In Table 4, the mean value, in *days*, of these distributions is reported for both protons and deuterons. From figure and table inspection, it is evident that the time spent in the heliosheath is greater, ranging from 2 to 5 times, than that spent in the inner heliosphere. This can be explained by the fact that the propagation in the heliosheath is performed with an almost pure diffusive 1D model where the other transport components are neglected or vastly reduced due to the absence of a definite HMF and a much slower solar wind speed (see discussion in Boschini et al., 2019). Moreover, in 2011, the modeled heliosheath had a larger depth compared to 2014 and 2018 (See Figures 4 and 5 in Boschini et al., 2019), resulting in a longer stochastic trajectory to reach the heliopause. This results is strictly connected with the discussion in Section 4.1. Indeed, the presence of the heliosheat has also a clear impact on code performances, it is necessary to include the great modulation effect observed at low energy by voyager probes (see, *e.g.*, Salvatore et al., 2025, and reference therein), but there is not a direct relationship between these two aspects. As a perspective, COSMICA would help in performing studies focused to have a clearer understanding of modulation process in the heliosheat. If we consider the propagation times in the inner heliosphere only, these are almost in agreement with those

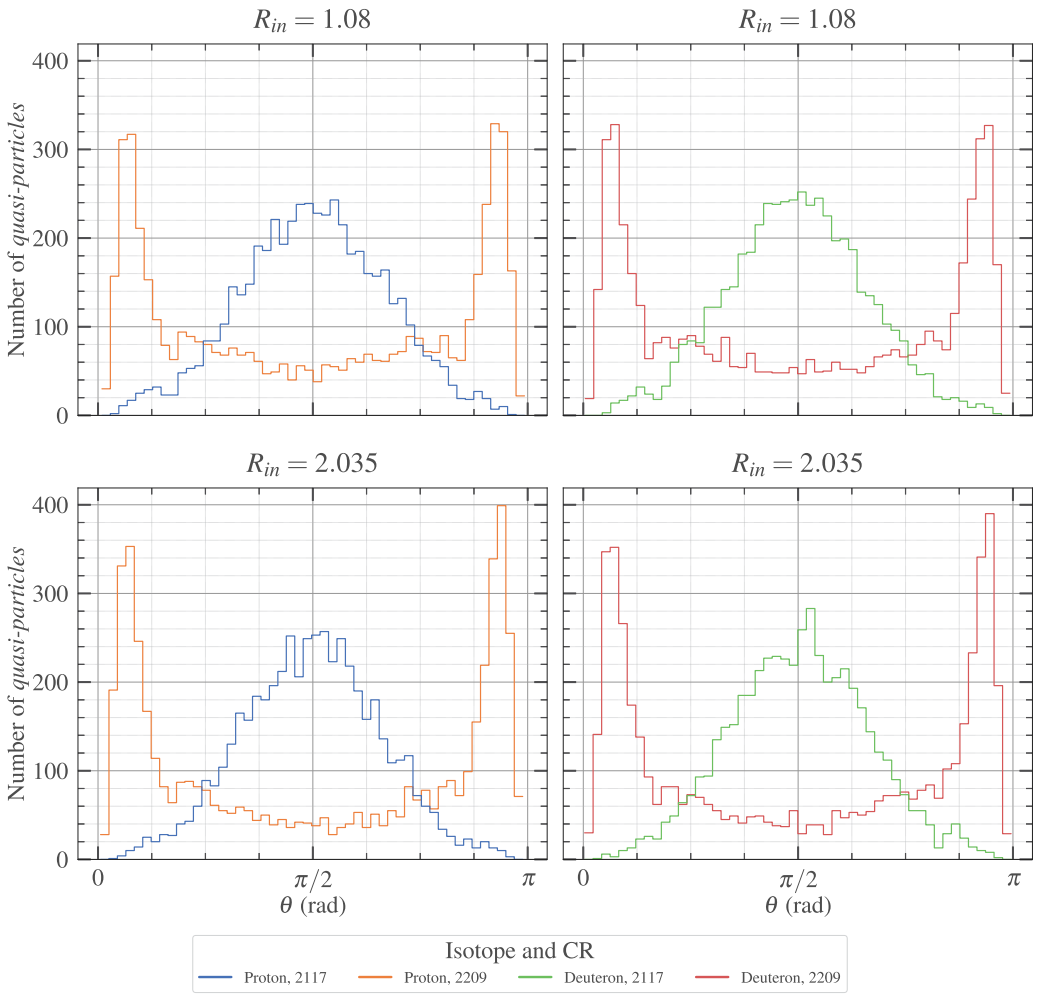

Fig. 6. Distribution of the exiting colatitude θ of the backward propagation of the simulated *quasi-particles*. Blue and green lines are referred to CR 2117, *i.e.*, solar minimum with negative heliospheric polarity. Orange and Red are referred to CR 2209, *i.e.*, solar minimum with positive heliospheric polarity.

Table 4
Mean propagation time, in *days*, of *quasi-particles* in the inner heliosphere and in the heliosheath.

CR	Proton		Deuteron	
	Inner	Heliosheath	Inner	Heliosheath
2117	88.87	438.71	77.52	409.44
2155	98.25	177.14	92.55	171.83
2209	51.27	174.19	39.97	140.17

presented by Tomassetti et al. (2025), where for cosmic protons and antiprotons with a kinetic energy of 1 GeV (~1.7 GV), they estimate a mean propagation time in the heliosphere of ~31–54 days during solar minimum and ~58–91 days during solar maxima. Our results are slightly greater, probably due to (a) the different rigidity of the calculation and (b) the effect of the contribution of reentrant particles from the heliosheath. Indeed, the lower the rigidity, the longer the propagation time in the inner heliosphere. The effect of re-entrant particles can be more understood by looking the relative resident time in the different zones of the heliosphere.

Fig. 8 reports the mean resident time in each sector in which we divide the heliosphere (see Section 2.1), for two solar minima and a solar maxima. As expected, solar maxima have, in general, higher resident time which reflect the fact that solar modulation is stronger during such periods. Zones 1 and 2 (*i.e.*, the space region between about 6~24 AU) show a higher resident time at solar maxima and HMF negative solar minima, while the resident time is more flat during HMF positive solar minima. These different distribution causes different solar modulation intensities even with similar average resident times: in fact, the rigidity loss term in Eq. (1) is proportional to $1/r$ (see Equation A.13 in Boschini et al., 2018b), thus, rigidity loss is more important closer to the sun regarding far distances. In all cases, an increase of resident time is observed in the last zone, where re-entrant events may occur. Re-entrant events are those *quasi-particle* events that, after passing the termination shock and spending few time in the heliosheat, pass again the termination shock *re-entering* into the inner heliosphere (see, *e.g.*, Bobik et al., 2008) increasing the total resident time computed in Fig. 7. This process adds further energy gain to the backward-in-time stochastic path which, in turn, increase the modulation effect and is more effective to lower rigidities. Finally, it is interesting to note that, in the most internal zone, where Earth-orbiting detectors are located, the mean time is on the order of a few days. When considering the most probable value, since the time distribution is strongly asymmetric, *quasi-particles* reside in this zone for ~7 days during solar maximum, ~3 days during HMF negative minima, and less than 1 day during the whole HMF positive descending phase and solar minima.

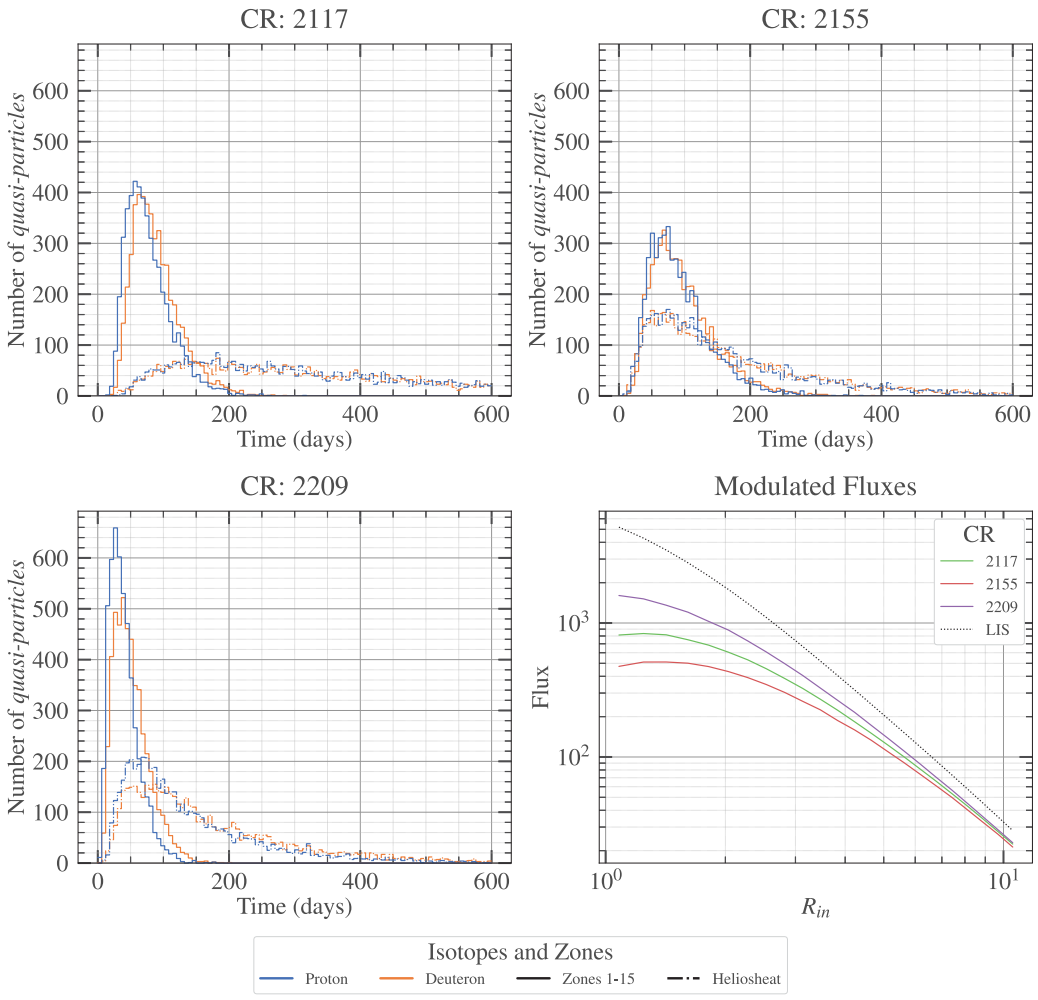

Fig. 7. *top row and lower left panel*: resident time distribution of *quasi-particle* below the termination shock (solid lines) and inside the heliosheat (dashed lines) for three different solar conditions: solar minimum with negative HMF polarity (CR 2117), solar maximum (CR 2155), and solar minimum with positive HMF polarity (CR 2209). Results are displayed for proton and deuterium isotopes at ∼1 GV. *Bottom right panel*: corresponding modulated spectra.

6. Conclusions

In this second part of the COSMICA study, which follows after Bacciu et al. (2026), we validated the GPU-accelerated Monte Carlo SDE solver against a well-established benchmark model of cosmic-ray modulation. By adopting the physical framework of HelMod-4/CUDA, which has been extensively tested against experimental data from AMS-02, PAMELA, and Voyager, we demonstrated that COSMICA reproduces the expected fluxes with excellent accuracy across different solar activity phases and heliospheric configurations. Statistical comparisons confirm that discrepancies between COSMICA and HelMod-4/CUDA outputs are consistent with stochastic fluctuations, without evidence of systematic deviations.

The benchmarking campaign revealed several key findings. First, COSMICA achieves speedups exceeding 100× for small workloads and stabilizes at ∼12× under large-scale saturation conditions, confirming the efficiency of its optimized scheduling and particle-ordering strategies. When applied to multi-GPU systems, scalability remains close to ideal, with four A100 GPUs delivering up to ∼120× speedup. This performance leap reduces month-long simulation campaigns to timescales of hours, enabling systematic parameter scans and real-time exploration of solar modulation scenarios.

Beyond confirming numerical accuracy, COSMICA's SDE formulation allows access to physical observables not readily derived in deterministic approaches. We analyzed the distributions of quasi-particle exit points, propagation times, and residence times, observing clear signatures of charge-sign dependent drifts and solar polarity reversals. These results reproduce well-known features of GCR transport, such as the asymmetric access to the inner heliosphere and the enhanced residence times within the heliosheath. Such analyses highlight the added scientific value of the Monte Carlo approach, where the ensemble of stochastic trajectories encodes rich information about the underlying transport processes.

The validation presented here consolidates COSMICA as a robust and reliable platform for cosmic-ray modulation studies. Its open-source availability, combined with its computational efficiency, make it suitable to be executed even on commercial computer with performances that previously were achieved only by using national supercomputing facilities. Looking ahead, COSMICA's modular structure will facilitate the integration of alternative transport models, non-standard heliospheric conditions, and additional physical effects such as local sources or energy losses. With this foundation, COSMICA is positioned to serve not only as a state-of-the-art numerical solver but also as a flexible research environment for addressing new challenges in space weather prediction, cosmic-ray astrophysics, and radiation hazard assessment for space missions.

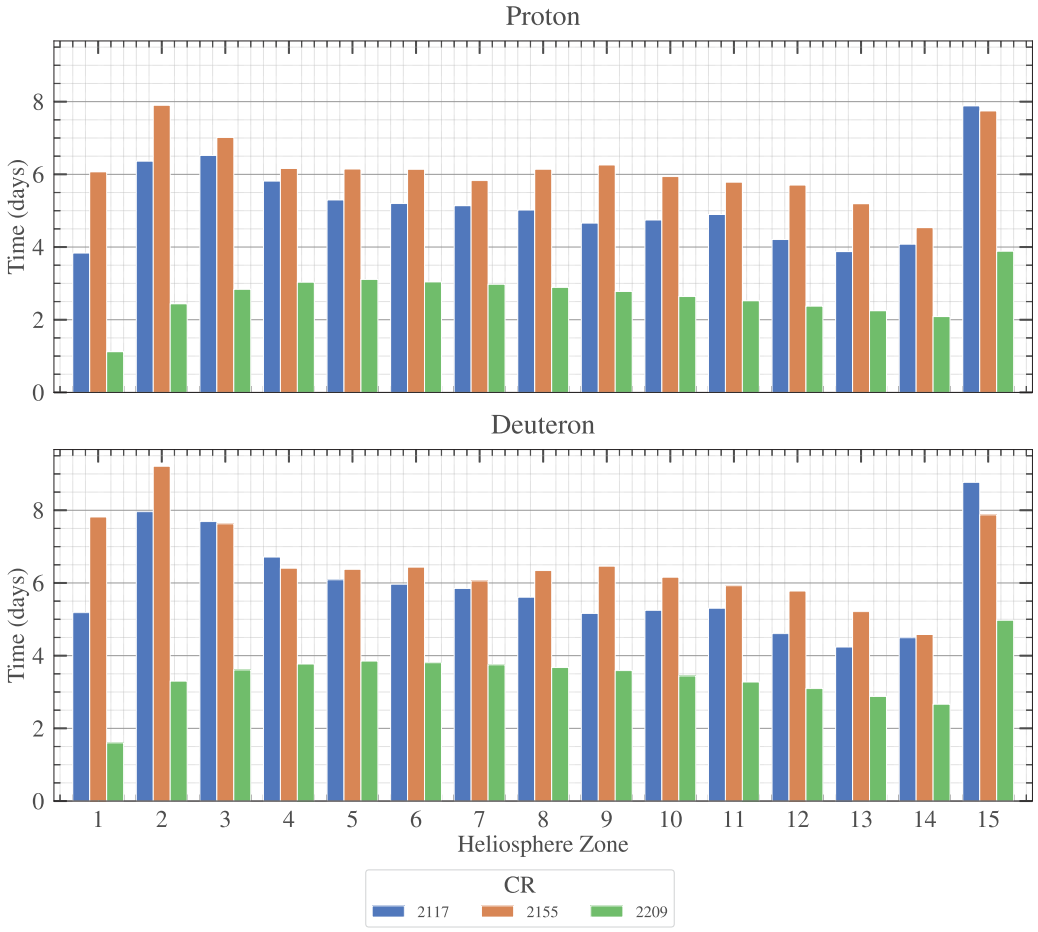

Fig. 8. Mean resident time (in days) in the different zones of the heliosphere for proton (top panel) and deuteron (bottom panel).

CRediT authorship contribution statement

Stefano Della Torre: Writing – review & editing, Writing – original draft, Supervision, Methodology, Investigation, Funding acquisition, Formal analysis, Conceptualization. **Leone Bacciu:** Writing – review & editing, Writing – original draft, Visualization, Software. **Matteo Grazioso:** Writing – review & editing, Writing – original draft, Visualization, Software. **Giovanni Cavallotto:** Writing – review & editing, Writing – original draft, Formal analysis, Conceptualization. **Massimo Gervasi:** Writing – review & editing, Resources. **Giuseppe La Vacca:** Writing – review & editing, Formal analysis. **Sabina Rossi:** Writing – review & editing, Supervision. **Marco S. Nobile:** Writing – review & editing, Supervision, Project administration, Funding acquisition.

Declaration of competing interest

The authors declare the following financial interests/personal relationships which may be considered as potential competing interests: Marco S. Nobile reports financial support was provided by Ca' Foscari University of Venice. If there are other authors, they declare that they have no known competing financial interests or personal relationships that could have appeared to influence the work reported in this paper.

Acknowledgments

This activity is supported by Fondazione ICSC, Spoke 3 Astrophysics and Cosmos Observations. National Recovery and Resilience Plan (Piano Nazionale di Ripresa e Resilienza, PNRR) Project ID *CN_*00000013. MG, SDT and GLV are supported by INFN and ASI under ASI-INFN Agreement No. 2019-19-HH.0 and its amendments and by ASIF implementation agreement No. 2021–36-HH.0 involving ASI and Milano-Bicocca University.

The project *"SDEGnO – Optimization and performances testing of CUDA-(multi) GPU-accelerated codes for the automatic parameterization of physical models based on SDE Monte Carlo algorithms"* is funded through the *"Bando a Cascata"* issued by Spoke 3 Astrophysics and Cosmos Observations, under the National Recovery and Resilience Plan (*Piano Nazionale di Ripresa e Resilienza*, PNRR, Project ID CN_00000013, Spoke Leader: Istituto Nazionale di Astrofisica – INAF, CUP C53C22000350006), and is carried out under the Agreement Rep. 531/2024 Prot. 283696/2024 between INAF and Ca' Foscari University of Venice.

This work was also supported by the high-performance computing infrastructure developed under the project "CONVECS", funded by the PR Veneto FESR 2021–2027 program, Priority 1 – Specific Objective 1.1 – Action 1.1.2.

The authors thank Alessandro Miotti for generously providing access to a desktop workstation equipped with an NVIDIA RTX 3090 GPU.

We acknowledge the NMDB database (www.nmdb.eu), founded under the European Union's FP7 programme (contract no. 213007) for providing data.

We acknowledge the ICSC for awarding this project access to the EuroHPC supercomputer LEONARDO, hosted by CINECA (Italy).

References

Abdo, A.A., Ackermann, M., Ajello, M., et al., 2009. Measurement of the cosmic ray $e^+ + e^-$ spectrum from 20 GeV to 1 TeV with the Fermi large area telescope. Phys. Rev. Lett. 102 (18), 181101. doi:10.1103/PhysRevLett.102.181101, arXiv:0905.0025.

Adriani, O., Barbarino, G.C., Bazilevskaya, G.A., et al., 2009. An anomalous positron abundance in cosmic rays with energies 1.5–100 GeV. Nature 458, 607–609. doi:10.1038/nature07942, arXiv:0810.4995.

Aguilar, M., Ali Cavasonza, L., Alpat, B., et al., 2021. Periodicities in the daily proton fluxes from 2011 to 2019 measured by the alpha magnetic spectrometer on the international space station from 1 to 100 GV. Phys. Rev. Lett. 127 (27), 271102. doi:10.1103/PhysRevLett.127.271102.

Aguilar, M., Ambrosi, G., Anderson, H., Arruda, L., et al., AMS Collaboration, 2025. Antiprotons and elementary particles over a solar cycle: Results from the alpha magnetic spectrometer. Phys. Rev. Lett. 134, 051002. doi:10.1103/PhysRevLett.134.051002.

Alvey, J., Bringmann, T., Kolesova, H., 2023. No room to hide: implications of cosmic-ray upscattering for GeV-scale dark matter. J. High Energy Phys. 2023 (1), 123. doi:10.1007/JHEP01(2023)123, arXiv:2209.03360.

Bacciu, L., Grazioso, M., Cavallotto, G., Della Torre, S., Gervasi, M., La Vacca, G., Rossi, S., Nobile, M.S., 2026. Massive stochastic simulation of cosmic rays propagation in the heliosphere: The COSMICA code. Astron. Comput. 55, 101043. doi:10.1016/j.ascom.2025.101043, URL: https://www.sciencedirect.com/science/article/pii/S2213133725001167.

Bacciu, L., et al., 2025. COSMICA repository. URL: https://github.com/ICSC-Spoke3/Cosmica-dev.

Bartocci, S., Sparvoli, R., Picozza, P., et al., 2020. Galactic cosmic-ray hydrogen spectra in the 40–250 MeV range measured by the high-energy particle detector (HEPD) on board the CSES-01 satellite between 2018 and 2020. Astrophys. J. 901 (1), 8. doi:10.3847/1538-4357/abad3e.

Royal Observatory of Belgium, B., 2025. WDC-SILSO. doi:10.24414/qnza-ac80, URL: https://www.sidc.be/SILSO/datafiles.

Bobik, P., Boella, G., Boschini, M.J., Consolandi, C., Della Torre, S., Gervasi, M., Grandi, D., Kudela, K., Pensotti, S., Rancoita, P.G., Rozza, D., Tacconi, M., 2013. Latitudinal dependence of cosmic rays modulation at 1 AU and interplanetary magnetic field polar correction. Adv. Astron. 2013 (1), 793072. doi:10.1155/2013/793072.

Bobik, P., Boella, G., Boschini, M.J., Consolandi, C., Torre, S.D., Gervasi, M., Grandi, D., Kudela, K., Pensotti, S., Rancoita, P.G., Tacconi, M., 2012. Systematic investigation of solar modulation of galactic protons for solar cycle 23 using a Monte Carlo approach with particle drift effects and latitudinal dependence. Astrophys. J. 745 (2), 132. doi:10.1088/0004-637X/745/2/132.

Bobik, P., Boella, G., Boschini, M.J., et al., 2012. Systematic investigation of solar modulation of galactic protons for solar cycle 23 using a Monte Carlo approach with particle drift effects and latitudinal dependence. Astrophys. J. 745, 132. doi:10.1088/0004-637X/745/2/132.

Bobik, P., Boschini, M.J., Consolandi, C., Torre, S.D., Gervasi, M., Grandi, D., Kudela, K., Vacca, G.L., Mandolesi, N., Rancoita, P.G., Rozza, D., Tacconi, M., 2016. On the forward-backward-in-time approach for Monte Carlo solution of Parker's transport equation: One-dimensional case. J. Geophys. Res.: Space Phys. 121 (5), 3920–3930. doi:10.1002/2015JA022237.

Bobik, P., Kudela, K., Boschini, M., Grandi, D., Gervasi, M., Rancoita, P., 2008. Solar modulation model with reentrant particles. Adv. Space Res. 41 (2), 339–342. doi:10.1016/j.asr.2007.02.085.

Boschini, M.J., Cavallotto, G., Della Torre, S., Gervasi, M., La Vacca, G., Rancoita, P.G., Tacconi, M., 2024. Fast and accurate evaluation of deep-space galactic cosmic ray fluxes with HelMod-4/CUDA. Adv. Space Res. 74 (9), 4302–4320. doi:10.1016/j.asr.2024.04.021.

Boschini, M.J., Della Torre, S., Gervasi, M., Grandi, D., Jóhannesson, G., La Vacca, G., Masi, N., Moskalenko, I.V., Pensotti, S., Porter, T.A., Quadrani, L., Rancoita, P.G., Rozza, D., Tacconi, M., 2018a. Deciphering the local interstellar spectra of primary cosmic-ray species with HelMod. Astrophys. J. 858 (1), 61. doi:10.3847/1538-4357/aabc54.

Boschini, M.J., Della Torre, S., Gervasi, M., Grandi, D., Jóhannesson, G., La Vacca, G., Masi, N., Moskalenko, I.V., Pensotti, S., Porter, T.A., Quadrani, L., Rancoita, P.G., Rozza, D., Tacconi, M., 2020a. Inference of the local interstellar spectra of cosmic-ray nuclei $Z \leq 28$ with the GalProp–HelMod framework. Astrophys. J. Suppl. Ser. 250 (2), 27. doi:10.3847/1538-4365/aba901.

Boschini, M.J., Della Torre, S., Gervasi, M., Grandi, D., Jóhannesson, G., La Vacca, G., Masi, N., Moskalenko, I., Pensotti, S., Porter, T., Quadrani, L., Rancoita, P., Rozza, D., Tacconi, M., 2022a. A hint of a low-energy excess in cosmic-ray fluorine. Astrophys. J. 925 (2), 108. doi:10.3847/1538-4357/ac313d, arXiv:2106.01626.

Boschini, M.J., Della Torre, S., Gervasi, M., Grandi, D., Jóhannesson, G., La Vacca, G., Masi, N., Moskalenko, I., Pensotti, S., Porter, T., Quadrani, L., Rancoita, P., Rozza, D., Tacconi, M., 2022b. Spectra of cosmic ray sodium and aluminum and unexpected aluminum excess. Astrophys. J. arXiv:2202.09928. Accepted. arXiv:2202.09928.

Boschini, M.J., Della Torre, S., Gervasi, M., La Vacca, G., Rancoita, P.G., 2018b. Propagation of cosmic rays in heliosphere: The HelMod model. Adv. Space Res. 62 (10), 2859–2879. doi:10.1016/j.asr.2017.04.017.

Boschini, M.J., Della Torre, S., Gervasi, M., La Vacca, G., Rancoita, P.G., 2019. The HelMod model in the works for inner and outer heliosphere: From AMS to voyager probes observations. Adv. Space Res. 64 (12), 2459–2476. doi:10.1016/j.asr.2019.04.007.

Boschini, M.J., Della Torre, S., Gervasi, M., La Vacca, G., Rancoita, P., 2022c. The transport of galactic cosmic rays in heliosphere: The HelMod model compared with other commonly employed solar modulation models. Adv. Space Res. 70 (9), 2636–2648. doi:10.1016/j.asr.2022.03.026.

Boschini, M.J., Della Torre, S., Gervasi, M., et al., 2017. Solution of heliospheric propagation: Unveiling the local interstellar spectra of cosmic-ray species. Astrophys. J. 840, 115. doi:10.3847/1538-4357/aa6e4f.

Boschini, M.J., Della Torre, S., Gervasi, M., et al., 2018c. HELMOD in the works: From direct observations to the local interstellar spectrum of cosmic-ray electrons. Astrophys. J. 854 (2), 94. doi:10.3847/1538-4357/aaa75e.

Boschini, M.J., Della Torre, S., Gervasi, M., et al., 2020b. Deciphering the local interstellar spectra of secondary nuclei with the Galprop/Helmod framework and a hint for primary lithium in cosmic rays. Astrophys. J. 889 (2), 167. doi:10.3847/1538-4357/ab64f1.

Boschini, M.J., Della Torre, S., Gervasi, M., et al., 2021. The discovery of a low-energy excess in cosmic-ray iron: Evidence of the past supernova activity in the local bubble. Astrophys. J. 913 (1), 5. doi:10.3847/1538-4357/abf11c.

Bottino, A., Donato, F., Fornengo, N., et al., 1998. Which fraction of the measured cosmic-ray antiprotons might be due to neutralino annihilation in the galactic halo? Phys. Rev. D 58 (12), 123503. doi:10.1103/PhysRevD.58.123503, arXiv:astro-ph/9804137.

Burger, R.A., Krüger, T.P.J., Hitge, M., et al., 2008. A Fisk–Parker hybrid heliospheric magnetic field with a solar-cycle dependence. Astrophys. J. 674, 511–519. doi:10.1086/525039.

Cernuda, I., 2011. Anisotropies in the cosmic-ray electron spectrum: A way to discriminate between exotic and astrophysical sources? In: Giani, S., Leroy, C., Rancoita, P.G. (Eds.), Cosmic Rays for Particle and Astroparticle Physics. pp. 513–518. doi:10.1142/9789814329033_0063.

Chang, J., Adams, J.H., Ahn, H.S., et al., 2008. An excess of cosmic ray electrons at energies of 300–800 GeV. Nature 456, 362–365. doi:10.1038/nature07477.

Cirelli, M., Cline, J.M., 2010. Can multistate dark matter annihilation explain the high-energy cosmic ray lepton anomalies? Phys. Rev. D 82 (2), 023503. doi:10.1103/PhysRevD.82.023503, arXiv:1005.1779.

database, N., 2025. NEST official release. URL: https://www.nmdb.eu/nest/.

Della Torre, S., Bobik, P., Boschini, M.J., et al., 2012. Effects of solar modulation on the cosmic ray positron fraction. Adv. Space Res. 49, 1587–1592. doi:10.1016/j.asr.2012.02.017.

Della Torre, S., Cavallotto, G., La Vacca, G., Gervasi, M., 2025. General properties of charged particle diffusion in heliosphere inferred from Forbush decreases. Adv. Space Res. doi:10.1016/j.asr.2025.04.053.

Della Torre, S., Gervasi, M., Rancoita, P.G., et al., 2015. Pulsar wind nebulae as a source of the observed electron and positron excess at high energy: The case of Vela-X. J. High Energy Astrophys. 8, 27–34. doi:10.1016/j.jheap.2015.08.001, arXiv:1508.01457.

Dunzlaff, P., Heber, B., Kopp, A., Rother, O., Müller-Mellin, R., Klassen, A., Gómez-Herrero, R., Wimmer-Schweingruber, R., 2008. Observations of recurrent cosmic ray decreases during solar cycles 22 and 23. Ann. Geophys. 26 (10), 3127–3138. doi:10.5194/angeo-26-3127-2008.

Dunzlaff, P., Strauss, R.D., Potgieter, M.S., 2015. Solving Parker's transport equation with stochastic differential equations on GPUs. Comput. Phys. Comm. 192, 156–165. doi:10.1016/j.cpc.2015.03.008.

Dunzlaff, P., Strauss, R., Potgieter, M., 2015. Solving Parker's transport equation with stochastic differential equations on GPUs. Comput. Phys. Comm. 192, 156–165. doi:10.1016/j.cpc.2015.03.008.

Effenberger, F., Fichtner, H., Scherer, K., Büsching, I., 2012. Anisotropic diffusion of galactic cosmic ray protons and their steady-state azimuthal distribution. Astron. Astrophys. 547, A120. doi:10.1051/0004-6361/201220203, arXiv:1210.1423.

Engelbrecht, N.E., Effenberger, F., Florinski, V., Potgieter, M.S., Ruffolo, D., Chhiber, R., Usmanov, A.V., Rankin, J.S., Els, P.L., 2022. Theory of cosmic ray transport in the heliosphere. Space Sci. Rev. 218 (4), 33. doi:10.1007/s11214-022-00896-1.

Engelbrecht, N.E., Strauss, R.D., le Roux, J.A., Burger, R.A., 2017. Toward a greater understanding of the reduction of drift coefficients in the presence of turbulence. Astrophys. J. 841 (2), 107. doi:10.3847/1538-4357/aa6f0e.

Ferreira, S.E.S., Potgieter, M.S., 2004. Long-term cosmic-ray modulation in the heliosphere. Astrophys. J. 603 (2), 744–752. doi:10.1086/381649.

Florinski, V., Pogorelov, N.V., 2009. Four-dimensional transport of galactic cosmic rays in the outer heliosphere and heliosheath. Astrophys. J. 701, 642–651. doi:10.1088/0004-637X/701/1/642.

Freidlin, M., 1985. Functional Integration and Partial Differential Equations. In: Annals of Mathematics Studies, Number No. 109, Princeton University Press.

Gardiner, C.W., 1985. Handbook of Stochastic Methods: for Physics, Chemistry and the Natural Sciences. Springer, doi:10.1007/978-3-662-02452-2.

Gardiner, C., 2009. Stochastic Methods : A Handbook for the Natural and Social Sciences. Springer Berlin, Heidelberg.

Gieseler, J., Heber, B., 2016. Spatial gradients of GCR protons in the inner heliosphere derived from ulysses COSPIN/KET and PAMELA measurements. Astron. Astrophys. 589, A32. doi:10.1051/0004-6361/201527972, arXiv:1602.00533.

Golge, S., O'Neill, P.M., Slaba, T.C., 2015. NASA galactic cosmic radiation environment model: Badhwar - O'Neill (2014). In: The 34th International Cosmic Ray Conference. PoS(ICRC2015)180.

Hattingh, M., Burger, R.A., 1995. A new simulated wavy neutral sheet drift model. Adv. Space Res. 16 (9), 213–216.
Higham, D.J., 2001. An algorithmic introduction to numerical simulation of stochastic differential equations. SIAM Rev. 43 (3), 525–546. doi:10.1137/S0036144500378302.
Hoeksema, J.T., 1995. The large-scale structure of the heliospheric current sheet during the ULYSSES epoch. Space Sci. Rev. 72, 137–148. doi:10.1007/BF00768770.
Ibarra, A., Tran, D., Weniger, C., 2010. Decaying dark matter in light of the PAMELA and Fermi LAT data. J. Cosmol. Astropart. P. 1, 009. doi:10.1088/1475-7516/2010/01/009, arXiv:0906.1571.
Jokipii, J.R., Kóta, J., 1989. The polar heliospheric magnetic field. Geophys. Res. Lett. 16 (1), 1–4. doi:10.1029/GL016i001p00001.
Jokipii, J.R., Levy, E.H., Hubbard, W.B., 1977. Effects of particle drift on cosmic-ray transport. I - General properties, application to solar modulation. Astrophys. J. 213, 861–868. doi:10.1086/155218.
Jokipii, J.R., Thomas, B., 1981. Effects of drift on the transport of cosmic rays. IV - modulation by a wavy interplanetary current sheet. Astrophys. J. 243, 1115–1122. doi:10.1086/158675.
Kappl, R., 2016. Solarprop: Charge-sign dependent solar modulation for everyone. Comput. Phys. Comm. 207, 386–399. doi:10.1016/j.cpc.2016.05.025.
King, J.H., Papitashvili, N.E., 2020. OMNI 27-day data set. doi:10.48322/NMH3-JF75, URL: https://omniweb.gsfc.nasa.gov/.
Kopp, A., Büsching, I., Strauss, R.D., Potgieter, M.S., 2012. A stochastic differential equation code for multidimensional Fokker–Planck type problems. Comput. Phys. Comm. 183 (3), 530–542. doi:10.1016/j.cpc.2011.11.014.
Kroese, D.P., Taimre, T., Botev, Z.I., 2011. Handbook of Monte Carlo Methods. Wiley, doi:10.1002/9781118014967.
Langner, U.W., Potgieter, M.S., 2004. Solar wind termination shock and heliosheath effects on the modulation of protons and antiprotons. J. Geophys. Res.: Space Phys. 109 (A1), doi:10.1029/2003JA010158.
Leroy, C., Rancoita, P.-G., 2011. Principles of Radiation Interaction in Matter and Detection, third ed. World Scientific, doi:10.1142/8200.
Liu, W., Guo, J., Wang, Y., Slaba, T.C., 2024. A comprehensive comparison of various galactic cosmic-ray models to the state-of-the-art particle and radiation measurements. Astrophys. J. Suppl. Ser. 271 (1), 18. doi:10.3847/1538-4365/ad1f2c.
Martucci, M., Munini, M., Boezio, M., et al., 2018. Proton fluxes measured by the PAMELA experiment from the minimum to the maximum solar activity for solar cycle 24. Astrophys. J. 854 (1), L2. doi:10.3847/2041-8213/aaa9b2.
Mertsch, P., Sarkar, S., 2011. The 'PAMELA anomaly' indicates a nearby cosmic ray accelerator. In: Giani, S., Leroy, C., Rancoita, P.G. (Eds.), Cosmic Rays for Particle and Astroparticle Physics. pp. 535–543. doi:10.1142/9789814329033_0066, arXiv:1108.1753.
Moloto, K., Engelbrecht, N., Strauss, R., Moeketsi, D., Van den Berg, J., 2019. Numerical integration of stochastic differential equations: A parallel cosmic ray modulation implementation on Africa's fastest computer. Adv. Space Res. 63 (2), 626–639. doi:10.1016/j.asr.2018.08.048.
Moloto, K.D., Engelbrecht, N.E., Strauss, R.D., Moeketsi, D.M., van den Berg, J.P., 2019. Numerical integration of stochastic differential equations: A parallel cosmic ray modulation implementation on Africa's fastest computer. Adv. Space Res. 63 (1), 626–639. doi:10.1016/j.asr.2018.08.048.
Moraal, H., 2014. Cosmic rays in the heliosphere: Observations. Astropart. Phys. 53, 175–185. doi:10.1016/j.astropartphys.2013.03.002, Centenary of cosmic ray discovery.
Nndanganeni, R.R., Potgieter, M.S., 2018. The global modulation of Galactic and Jovian electrons in the heliosphere. Astrophys. Space Sci. 363 (7), 156. doi:10.1007/s10509-018-3377-z.
Observatory, T.W.S., 1995. WSO solar magnetic field observations. URL: http://wso.stanford.edu/.
Øksendal, B., 2010. Stochastic Differential Equations: An Introduction with Applications. In: Universitext, Springer Berlin Heidelberg.
Parker, E.N., 1965. The passage of energetic charged particles through interplanetary space. Plan. Space Sci. 13, 9–49. doi:10.1016/0032-0633(65)90131-5.
Peter, J.S., Schuemann, J., Held, K.D., McNamara, A.L., 2022. Nano-scale simulation of neuronal damage by galactic cosmic rays. Phys. Med. Biol. 67 (23), 235001. doi:10.1088/1361-6560/ac95f4, arXiv:2202.07547.
Potgieter, M.S., 1998. The modulation of galactic cosmic rays in the heliosphere: Theory and models. Space Sci. Rev. 83 (1), 147–158. doi:10.1023/A:1005014722123.
Potgieter, M.S., Ferreira, S.E.S., 2001. Modulation of cosmic rays in the heliosphere: theory and models. In: 27th International Cosmic Ray Conference. ICRC27, In: International Cosmic Ray Conference, vol. 27, p. 217.
Potgieter, M.S., Moraal, H., 1985. A drift model for the modulation of galactic cosmic rays. Astrophys. J. 294 (part 1), 425–440. doi:10.1086/163309.
Qin, G., Shen, Z., 2017. Modulation of galactic cosmic rays in the inner heliosphere, comparing with PAMELA measurements. Astrophys. J. 846 (1), 56. doi:10.3847/1538-4357/aa83ad.
Raath, J.L., Potgieter, M.S., Strauss, R.D., et al., 2016. The effects of magnetic field modifications on the solar modulation of cosmic rays with a SDE-based model. Adv. Space Res. 57, 1965–1977. doi:10.1016/j.asr.2016.01.017, arXiv:1506.07305.
Rahmanian, S., Slaba, T.C., Braby, L.A., Santa Maria, S.R., Bhattacharya, S., Straume, T., 2023. Galactic cosmic ray environment predictions for the NASA BioSentinel mission. Life Sci. Space Res. 38, 19–28. doi:10.1016/j.lssr.2023.05.001.
Rankin, J., Bindi, V., Bykov, A., Cummings, A., Della Torre, S., Florinski, V., Heber, B., Potgieter, M., Stone, E., Zhang, M., 2022. Galactic cosmic rays throughout the heliosphere and in the very local interstellar medium. Space Sci. Rev. 218 (5), 42. doi:10.1007/s11214-022-00912-4.
Rankin, J.S., McComas, D.J., Leske, R.A., Christian, E.R., Cohen, C.M.S., Cummings, A.C., Joyce, C.J., Labrador, A.W., Mewaldt, R.A., Schwadron, N.A., Stone, E.C., Strauss, R.D., Wiedenbeck, M.E., 2022. Anomalous cosmic-ray oxygen observations into 0.1 au. Astrophys. J. 925 (1), 9. doi:10.3847/1538-4357/ac3c1e.
Rozza, D., Della Torre, S., Gervasi, M., et al., 2015. Vela-X as main contributor to the electron and positron spectra at energy above 100 GeV. In: The 34th International Cosmic Ray Conference. PoS(ICRC2015)501.
Salati, P., 2011. Charged cosmic rays from dark matter. In: Giani, S., Leroy, C., Rancoita, P.G. (Eds.), Cosmic Rays for Particle and Astroparticle Physics. pp. 613–625. doi:10.1142/9789814329033_0076.
Salvatore, S., Della Torre, S., Gervasi, M., La Vacca, G., Becker Tjus, J., 2025. Inferring the effective diffusion coefficient of galactic cosmic rays in the heliosheath. Adv. Space Res. 76 (8), 4781–4792. doi:10.1016/j.asr.2025.07.033.
Samwel, S.W., El-Aziz, E.A., Garrett, H.B., Hady, A.A., Ibrahim, M., Amin, M.Y., 2019. Space radiation impact on smallsats during maximum and minimum solar activity. Adv. Space Res. 64 (1), 239–251. doi:10.1016/j.asr.2019.03.025.
Shen, Z., Qin, G., Zuo, P., Wei, F., 2019. Modulation of galactic cosmic rays from helium to nickel in the inner heliosphere. Astrophys. J. 887 (2), 132. doi:10.3847/1538-4357/ab5520.
Solanik, M., Bobik, P., Genci, J., 2022. Cosmic rays modulation in heliosphere models on GPU. In: 37th International Cosmic Ray Conference. 12-23 July 2021. Berlin. p. 1320.
Solanik, M., Bobík, P., Genči, J., 2023. Geliosphere - parallel CPU and GPU based models of cosmic ray modulation in the heliosphere. Comput. Phys. Comm. 291, 108847. doi:10.1016/j.cpc.2023.108847.
Strauss, R.D.T., Effenberger, F., 2017. A Hitch–Hiker's guide to stochastic differential equations. Space Sci. Rev. 212 (1–2), 151–192. doi:10.1007/s11214-017-0351-y.
Strauss, R.D.T., Effenberger, F., 2017. A Hitch–Hiker's guide to stochastic differential equations. Solution methods for energetic particle transport in space physics and astrophysics. Space Sci. Rev. 212 (1–2), 151–192. doi:10.1007/s11214-017-0351-y, arXiv:1703.06192.
Strauss, R.D., Potgieter, M.S., Boezio, M., Simone, N.D., Di Felice, V., Kopp, A., Busching, I., 2012. The heliospheric transport of protons and anti-protons: a stochastic modelling approach to pamela observations. doi:10.1142/9789814405072_0042.
Strauss, R.D., Potgieter, M.S., Büsching, I., Kopp, A., 2011a. Modeling the modulation of Galactic and Jovian electrons by stochastic processes. Astrophys. J. 735 (2), 83. doi:10.1088/0004-637X/735/2/83.
Strauss, R.D., Potgieter, M.S., Kopp, A., Büsching, I., 2011b. On the propagation times and energy losses of cosmic rays in the heliosphere. J. Geophys. Res.: Space Phys. 116 (A12), A12105. doi:10.1029/2011JA016831.
Tomassetti, N., Bertucci, B., Fiandrini, E., Khiali, B., 2025. Propagation times and energy losses of cosmic protons and antiprotons in interplanetary space. Galaxies 13 (2), 23. doi:10.3390/galaxies13020023.
Valdés-Galicia, J., 2005. Low energy galactic cosmic rays in the heliosphere. Adv. Space Res. 35 (5), 755–767. doi:10.1016/j.asr.2005.03.149, Fundamentals of Space Environment Science.
Vogt, A., Engelbrecht, N.E., Heber, B., Kopp, A., Herbst, K., 2022. Numerical and experimental evidence for a new interpretation of residence times in space. Astron. Astrophys. 657, A39. doi:10.1051/0004-6361/202038980, arXiv:2110.11213.
Vogt, A., Engelbrecht, N.E., Strauss, R.D., Heber, B., Kopp, A., Herbst, K., 2020. The residence-time of Jovian electrons in the inner heliosphere. Astron. Astrophys. 642, A170. doi:10.1051/0004-6361/201936897, arXiv:2006.16768.
Vogt, A., Heber, B., Kopp, A., Potgieter, M.S., Strauss, R.D., 2018. Jovian electrons in the inner heliosphere. Proposing a new source spectrum based on 30 years of measurements. Astron. Astrophys. 613, A28. doi:10.1051/0004-6361/201731736.
Weniger, C., 2011. Gamma-ray anisotropies from decaying dark matter. In: Giani, S., Leroy, C., Rancoita, P.G. (Eds.), Cosmic Rays for Particle and Astroparticle Physics. World Scientific, pp. 632–640. doi:10.1142/9789814329033_0078.
Zhang, M., 1999. A Markov stochastic process theory of cosmic-ray modulation. Astrophys. J. 513 (1), 409–420. doi:10.1086/306857.
Zhao, L.-L., Qin, G., Zhang, M., Heber, B., 2014. Modulation of galactic cosmic rays during the unusual solar minimum between cycles 23 and 24. J. Geophys. Res. (Space Phys.) 119 (3), 1493–1506. doi:10.1002/2013JA019550, arXiv:1310.7076.